

UC San Diego

UC San Diego Electronic Theses and Dissertations

Title

The flow in an under-floor plenum

Permalink

<https://escholarship.org/uc/item/4w21p6bq>

Author

Choi, Jun Myoung

Publication Date

2009

Peer reviewed|Thesis/dissertation

UNIVERSITY OF CALIFORNIA, SAN DIEGO

The Flow in an Under-Floor Plenum

A thesis submitted in partial satisfaction of the requirements
for the degree Master of Science

in

Engineering Science (Mechanical Engineering)

by

Jun Myoung Choi

Committee in charge:

Professor Paul F. Linden, Chair
Professor Forman A. Williams
Professor Kalyanasundaram Seshadri

2009

The Thesis of Jun Myoung Choi is approved and it is acceptable in quality and form for publication on microfilm and electronically:

Chair

University of California, San Diego
2009

To my wife, Ji Eun

and my son, Eun Jae

TABLE OF CONTENTS

SIGNATURE PAGE.....	iii
DEDICATION.....	iv
TABLE OF CONTENTS.....	v
LIST OF FIGURES.....	vii
LIST OF TABLES.....	xi
ABSTRACT OF THE THESIS.....	xii
1 INTRODUCTION.....	1
1.1 Introduction to an Under-floor Air Distribution (UFAD) System.....	1
1.2 Problem Statements and Objectives.....	2
1.3 Approaches.....	3
1.4 Overview.....	5
2 EXPERIMENTAL AND NUMERICAL METHODS.....	7
2.1 Experimental methods.....	7
2.2 Numerical methods.....	10
3 THE EFFECT OF FLOW RATE AND PLENUM DEPTH.....	15
3.1 Observations.....	15
3.2 Summary and discussions.....	25
4 THE EFFECT OF INLET AREA VARIATION.....	28
4.1 Observations.....	28
4.2 Summary and discussions.....	36
5 THE EFFECT OF INLET POSITION.....	40
5.1 Observations.....	40
5.2 Summary and discussions.....	43
6 THE EFFECT OF BUOYANCY.....	52

6.1	Observations.....	52
6.2	Summary and discussions.....	63
7	CONCLUSIONS.....	66
	REFERENCES.....	69

LIST OF FIGURES

Figure 1.1: UFAD system installed in a typical office.....	1
Figure 1.2: Under-floor plenum temperatures measured in a typical office building. The maximum temperature difference is 5.2F. Courtesy of F.Bauman.....	3
Figure 2.1: The schematic diagram of the experimental apparatus.....	8
Figure 2.2: The schematic of the under-floor plenum for experiments.....	8
Figure 2.3: Path lines and grid velocity vectors created by Pliolite particles.....	9
Figure 2.4: An Under-floor plenum in a typical room (a) and one-quarter plenum for computational domain.....	10
Figure 3.1: The flow patterns corresponding to the flow rates and plenum depths.....	16
Figure 3.2: Residence time distribution corresponding to flow rate ($H=0.2\text{m}$).....	17
Figure 3.3: Residence time distribution corresponding to flow rate ($H=0.3\text{m}$).....	18
Figure 3.4: Residence time distribution corresponding to flow rate ($H=0.4\text{m}$).....	18
Figure 3.5: The dependence of average residence time on flow rate	19
Figure 3.6: The dependence of average residence time with plenum depth.....	20
Figure 3.7: The dependence of dimensionless average residence time on aspect ratio.....	21
Figure 3.8: Average path length corresponding to flow rates and plenum depths.....	21
Figure 3.9: Comparison between volume averaged velocities and average velocities calculated from average residence time and path length.....	22
Figure 3.10: The change of Nu corresponding to Re	23
Figure 3.11: The dependence of STD of outlet temperature on plenum depth and flow rate.....	24
Figure 3.12: The dependence of temperature difference between maximum and minimum air temperature among diffusers on plenum depth and flow rate.....	24
Figure 3.13: Different residence time distributions caused by different plenum depths ($Q=0.035\text{m}^3/\text{s}$).....	26
Figure 3.14: The change of average temperature of 370 air particles with dimensionless residence time. Right axis indicates the number of Air particles remained in a plenum. ($H=0.4\text{m}$ and $Q=0.02\text{m}^3/\text{s}$).....	27

Figure 3.15: The change of STD of temperatures of 370 air particles with dimensionless residence time. Right axis indicates the number of Air particles remained in a plenum. ($H=0.4\text{m}$ and $Q=0.02\text{m}^3/\text{s}$).....	27
Figure 4.1: Plenum geometry and inlet configurations at each case (group A).....	28
Figure 4.2: The change of flow patterns and Nu contours depending on inlet configurations (group A).....	29
Figure 4.3: Plenum geometry and inlet configurations at each case (group B).....	30
Figure 4.4: The change of flow pattern and Nu contour depending on inlet configuration (group B).....	31
Figure 4.5: Residence time distribution corresponding to inlet configurations (A).....	32
Figure 4.6: Residence time distribution corresponding to inlet configurations (B).....	32
Figure 4.7: Average residence times depending on inlet area ($\tau=270\text{s}$).....	33
Figure 4.8: Path length distribution corresponding to inlet configurations (group A).....	34
Figure 4.9: Path length distribution corresponding to inlet configurations (group B).....	34
Figure 4.10: Average path lengths depending on inlet area.....	35
Figure 4.11: Average Nu depending on inlet configuration.....	35
Figure 4.12: STD of outlet temperatures depending on inlet configuration.....	36
Figure 4.13: The change of average temperature of 100 air particles with dimensionless residence time corresponding to Case 1, 3, 5, and 6. The inlet ID for open inlets are indicated in parenthesis in legend.....	37
Figure 4.14: The change of Nu with Re ($\tau=270\text{s}$).....	38
Figure 4.15: The behaviors of Nu and Re depending on replenishment time and inlet area.....	39
Figure 5.1: Case numbers corresponding to inlet positions.....	40
Figure 5.2: The dependence of flow patterns and Nu contours on inlet position.....	41
Figure 5.3: The dT and STD of outlet temperatures at each case.....	41
Figure 5.4: The change of Nu with Re ($\tau = 270\text{s}$).....	43
Figure 5.5: Flow pattern created by particle paths for the case 4.....	44
Figure 5.6: Inlet configurations for investigating the effect of number of vortex in a plenum.....	45

Figure 5.7:	The flow patterns and Nu contours corresponding to the number of vortices.....	45
Figure 5.8:	A perimeter of unit vortex at each case.....	46
Figure 5.9:	The change of dT and STD of outlet temperatures with the number of symmetrical vortices.....	46
Figure 5.10:	The change of distance from y-axis with residence time (Case 1).....	47
Figure 5.11:	The change of distance from y-axis with residence time (Case 2).....	48
Figure 5.12:	The change of distance from y-axis with residence time (Case 3).....	48
Figure 5.13:	The horizontal velocity profile and temperature distribution of flow at mid depth in Case 1 in Figure 5.7.....	49
Figure 5.14:	The contour of average residence time through diffusers for Case 1 in Figure 5.7. The spots at which lines are crossed indicate the diffusers. The range of average residence time is indicated in the legend.....	45
Figure 5.15:	The change of temperature of particles with time which escapes through diffuser A and B ($\tau = 270s$)	51
Figure 6.1:	The effect of gravity g on Nu corresponding to plenum depths.....	53
Figure 6.2:	Nu difference caused by buoyancy effect ($\tau = 270s$ or $Q=0.02m^3/s$)	55
Figure 6.3:	Nu difference caused by buoyancy effect ($\tau = 135s$ or $Q=0.04m^3/s$).....	56
Figure 6.4:	Nu difference caused by buoyancy effect ($\tau = 90s$ or $Q=0.06m^3/s$).....	57
Figure 6.5:	The buoyancy effect on the flow patterns ($\tau = 270s$ or $Q=0.02m^2$).....	58
Figure 6.6:	STD of outlet temperatures for gravity case and no gravity case ($\tau = 270s$ or $Q=0.02m^2$).....	59
Figure 6.7:	The buoyancy effect on the flow patterns ($\tau = 135s$ or $Q=0.04m^2$).....	60
Figure 6.8:	STD of outlet temperatures for gravity case and no gravity case ($\tau = 135s$ or $Q=0.04m^2$).....	61
Figure 6.9:	The buoyancy effect on the flow patterns ($\tau = 90s$ or $Q=0.06m^2$).....	62
Figure 6.10:	STD of outlet temperatures for gravity case and no gravity case ($\tau = 90s$ or $Q=0.06m^2$).....	63
Figure 6.11:	The flow patterns for Case 1 and 7 ($Q=0.02m^3/s$, buoyancy included).....	64
Figure 6.12:	The change of average temperature of 70 air particles with dimensionless residence time for case 1 and 7. The open inlet IDs are represented in parenthesis.....	65

Figure 7.1: The vertical velocity profiles and temperature distribution of flow at mid depth corresponding to the number of vortex.....67

LIST OF TABLES

Table 6.1: Inlet configurations and dimensionless groups corresponding to cases...54

ABSTRACT OF THE THESIS

The Flow in an Under-Floor Plenum

by

Jun Myoung Choi

Master of Science in Engineering Science (Mechanical Engineering)

University of California, San Diego, 2009

Professor Paul F. Linden, Chair

There is considerable growth in popularity of under-floor air distribution (UFAD) systems because of potential energy savings, an improvement in air quality, and thermal comfort over conventional systems. With these advantages, the UFAD system could be an alternative air distribution system potentially superior to traditional overhead system; however, well-developed design methodologies especially for under-floor plenum have not been fully explored. We have considered

two issues that lower the performance of under-floor plenum in UFAD system. One is the temperature difference between diffusers results in discomfort for occupants, and the other is the heat transfer across a slab lowers energy efficiency in UFAD system.

The Particle Tracking Velocimetry (PTV) experiment was conducted to demonstrate the flow pattern in the plenum, and the computational calculation by commercial FLUENT software was performed to show the flow patterns and physical properties of the flow.

In this thesis, the plenum of good performance is defined as the plenum that has lower temperature variation from diffuser to diffuser and lower heat transfer rate across a slab. The objectives of this thesis are to investigate the physical properties of flow in a plenum, and give ideas for reducing temperature variation of air leaving diffusers and heat transfer across a slab.

1 INTRODUCTION

1.1 Introduction to an under-floor air distribution (UFAD) system

There is considerable growth in popularity of UFAD systems because of potential energy savings, and potential improvement in air quality and thermal comfort over conventional air conditioning systems. The conventional overhead system supplies conditioned air from a ceiling-level register, and it is designed to mix this supply air with the room air to maintain the entire room at a certain desired temperature. In contrast, in a UFAD system, the conditioned air is introduced through diffusers placed in a raised floor, and it is designed to stratify the space with only the lower occupied zone maintained at the temperature set point.

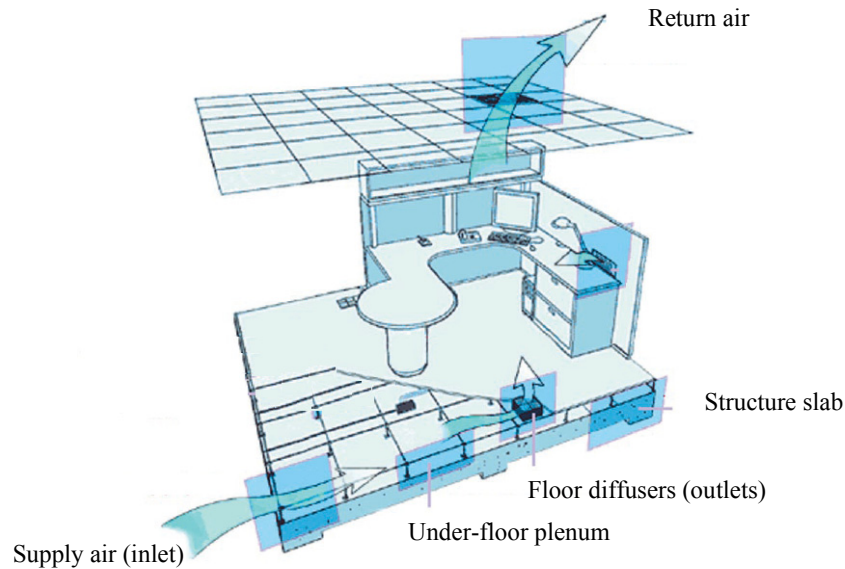


Figure 1.1: UFAD system installed in a typical office

There is no reliable evidence of overall energy savings over conventional overhead system; however, the number of buildings that have a UFAD system installed have increased recently because it provides several potential benefits. The direction of overall airflow is the same as that of thermal lift so that when indoor air

is contaminated it can be removed effectively. Also by allowing personal control of the local thermal environment, UFAD systems could satisfy nearly all occupants.

With these advantages the UFAD system is an alternative air distribution system, potentially superior to traditional overhead system; however, well developed design methodologies especially design for the air flow within the under-floor plenum have not been fully explored.

1.2 Problem statement and objectives

There are two major concerns with plenum design. One is temperature variations of outlet temperatures at different diffusers, and the other is heat transfer across the floor slab from return air in a lower story.

Since the return air in the space below the plenum is warmer than the air in the plenum, heat transfer through the floor slab heats the supply air before it enters a room. Consequently, the temperature of the air leaving the diffusers depends on the residence time and the path length of the air in the plenum. Measurement of temperatures in the plenum installed in a typical multistory building revealed that temperature variations of as much as 4°C can occur between different diffusers, and this problem can give significant discomfort to the occupants.

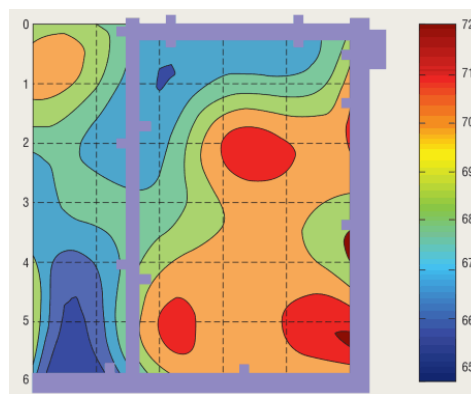


Figure 1.2: Under-floor plenum temperatures measured in a typical office building. The maximum temperature difference is 5.2F. Courtesy of F. Bauman

The heat transfer from the lower floor is inevitable unless the slab is thoroughly insulated. Previous with a simplified heat balance model estimates that 30%~40% of the total room cooling load is transferred into the supply plenum and only about 60%~70% is accounted for by the return air extraction rate (Bauman, 2006). Therefore, the heat transfer across a slab may offset the energy saving of UFAD obtained by stratification.

The first objective of this thesis is to observe the behaviors of flow with various independent factors, and second one is to give ideas how to reduce the temperature variation through diffusers and the heat transfer across a slab.

1.3 Approaches

With a plenum of height H and width L , we may assume the flow in a plenum is approximately two-dimensional fluid when the aspect ratio H/L is small. From the continuity equation

$$\frac{\partial u}{\partial x} + \frac{\partial w}{\partial z} = 0, \quad (\text{Equation 1.1})$$

the characteristic velocities and lengths can be related to each other by scaling analysis as

$$W \approx \frac{H}{L}U \quad (\text{Equation 1.2})$$

, where U and W are the scales of horizontal velocity u and vertical velocity w , respectively. Therefore, the vertical velocity scale W may be ignorable when the aspect ratio is small.

We consider two specific plenum configurations. Plenum A, whose size is $5.78 \times 5.78 \times 0.3\text{m}$, has two inlets which release supply air from the center of the

plenum, and 25 diffusers are located in the raised floor to introduce conditioned air to the room. The dimensions for plenum B are $3 \times 6 \times 0.3$ m, and it has 20 inlets and 72 outlets. Plenum B is used to investigate the effects of inlet position and inlet area. The overall shapes of the two plenums are described in Chapter 3.

A Particle Tracking Velocimetry (PTV) experiment was conducted to demonstrate the flow pattern, and computational calculations performed using the commercial FLUENT software were used to calculate the flow pattern and physical properties of the flow.

When conditioned air is supplied to the plenum, it is heated by heat transfer from the lower floor. Given isothermal boundary condition on the slab, the temperature variation of air as shown in Figure 1.2 presumably results from the different residence times or path lengths of air before it leaves the plenum. Consequently, the residence times and path lengths are considered as essential dependent parameters that can be associated with temperature variations of air entering the room from the different diffusers. The STD of air temperatures at the diffusers will be measured to investigate the temperature variation.

In a pure forced convection with fixed Prandtl number Pr , the Nusselt number Nu is a function of Reynolds number Re , and Nu increases with increase of Re . Therefore, in terms of heat transfer, Nu is a significant dependent parameter that indicates the fraction of the thermal energy of the return-air plenum in the lower story that is transferred to the under-floor plenum through the slab.

Observing these dependent parameters such as residence time, path length, STD of outlet temperatures, and Nu the performance of plenum was investigated through case studies with selections of flow rate, plenum depth, inlet area, and inlet

position as independent parameters. Also, the effects of natural convection and flow pattern are also studied.

1.4 Overview

In Chapter 2, we describe experimental techniques and show the flow pattern under a certain conditions by particle tracking velocimetry (PTV) experiments. We introduce the numerical calculations by FLUENT used to visualize the movements of particles and investigate the flow in terms of heat transfer..

In Chapter 3, we investigate the dependence of flow behavior in a plenum on the flow rate and plenum depth. Plenum A with depths of 0.2, 0.3, and 0.4m is used, and a wide range of ACH (air changes per hour) from 5 to 70 is used. With the aid of Matlab, the data imported from FLUENT was processed to calculate the average residence times and path lengths. Overall distribution curves of residence times and path lengths are determined. The average Nusselt number \overline{Nu} on the bottom surface of a plenum is also obtained.

In Chapter 4, we observe the flow behaviors when an inlet area is enlarged. Both plenum A and B are used. With plenum B which has 20 inlets we investigate the effect of inlet area which was varied by controlling the number of open inlets. Average residence time and path lengths are calculated along with their probability distributions. The flow patterns and \overline{Nu} contours on a bottom surface are obtained.

In Chapter 5, we focus the effect of inlet position. The different inlet positions results in different flow patterns. With the case studies, we tried to find a certain condition that decreases temperature variation over diffusers. Plenum B is used, and the inlet position is changed by switching the open inlets.

In Chapter 6, using both plenum A and B we check how the properties of flow are changed when buoyancy is taken into consideration. Previously we assumed two-dimensional flow when the plenum depth is small. As the plenum depth becomes deeper, the vertical component of velocity becomes important as the buoyancy force becomes significant. When buoyancy is included in the flow, the heat transfer driven by natural convection may become important under certain conditions. In this Chapter, we attempt to find a condition where buoyancy force may not be negligible, and observe the effects of buoyancy effect on temperature variation from diffuser to diffuser.

In Chapter 7, we summarize the behaviors of flow in a plenum by the various independent parameters, and associate them with a performance of a under-floor plenum in UFAD system.

2 EXPERIMENTAL AND NUMERICAL METHODS

2.1 Experimental methods

The PTV (particle tracking velocimetry) experiment was used to obtain velocity vectors of moving particles in the flow. In this thesis, the PTV experiment was conducted only to visualize the flow pattern for a specific plenum model.

In order to describe the flow in the plenum, we used a one-tenth scaled UFAD model in the laboratory. The internal dimensions of the tank are 59.7×59.7×45cm. The upper space in Figure 2.1 represents the under floor plenum, and the lower space represents a typical room. We used this upside down configuration because it offers clear view for the digital camera above the tank as shown in Figure 2.1. The 25 holes placed at the plate between the two spaces are represent the diffusers that distribute conditioned air into a room in a real UFAD system. Pliolite particles were used as tracer particles. The density of the particles is 1.021kg/m³, and salt water with the same density was placed in the tank in order for the particles to remain neutrally buoyant. A particle size of 800μm in diameter was used and prepared by sieving the particles through a mesh. Before releasing the particles into salt water in the tank, they were wetted with the aid of wetting agent. The slide projector was placed beside the tank to illuminate the particles in the plenum. A light slit was used to generate a thin horizontal light sheet.

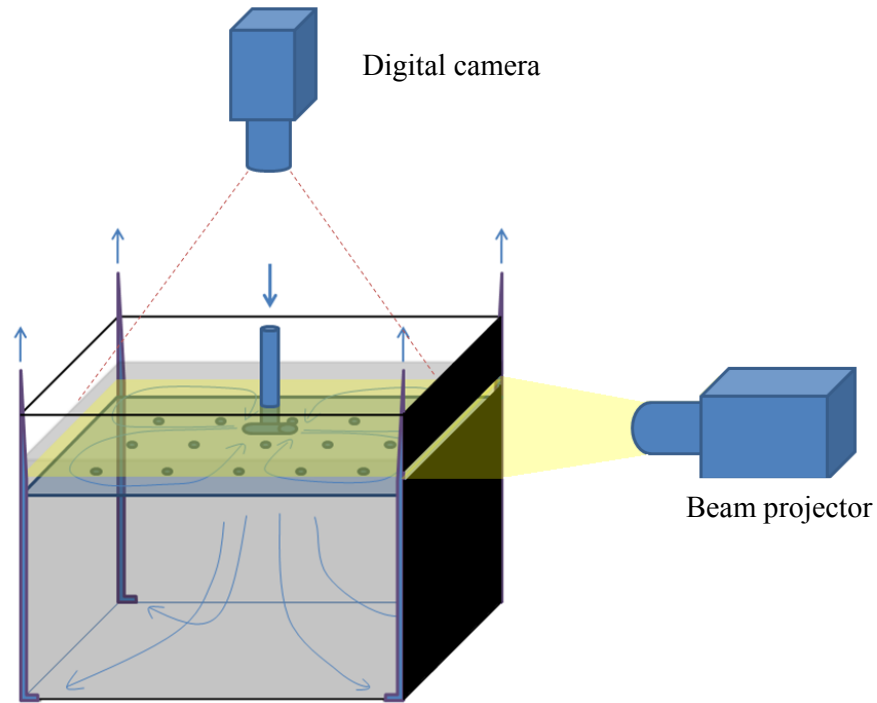


Figure 2.1: The schematic diagram of the experimental apparatus

We consider the flow in an under-floor plenum whose dimensions are $5.78 \times 5.78 \times 0.3\text{m}$ with 2 inlets and 25 diffusers. The two inlets were placed in the middle of the plenum, and they inject conditioned air in opposite directions to each other. This plenum is sketched in Figure 2.2.

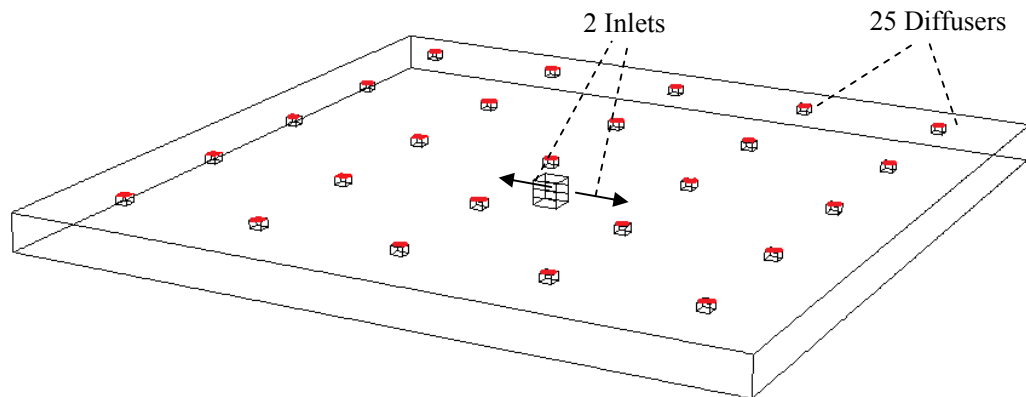


Figure 2.2: The schematic of the under-floor plenum for experiments

Salt water was added until the depth of water in the plenum reached 3cm. By using a peristaltic pump, the water in the tank was circulated from lower space to the plenum. Then, Pliolite particles were released in the upper layer. The horizontal light sheet of 3mm in width formed by the slide projector illuminates particles moving horizontally in the mid-plane of the plenum. A digital camera above a tank captured the movement of particles, and the horizontal trajectories were visualized through image processing by Digiflow. The path lines and grid velocity vector contour created by Digiflow represent a symmetric flow pattern as shown in Figure 2.3. The Reynolds number $Re=Ud/v$ is calculated from the mean volume flow rate, inner diameter of orifice d , and kinematic viscosity v . The Re of the source jet was around order of 10^2 .

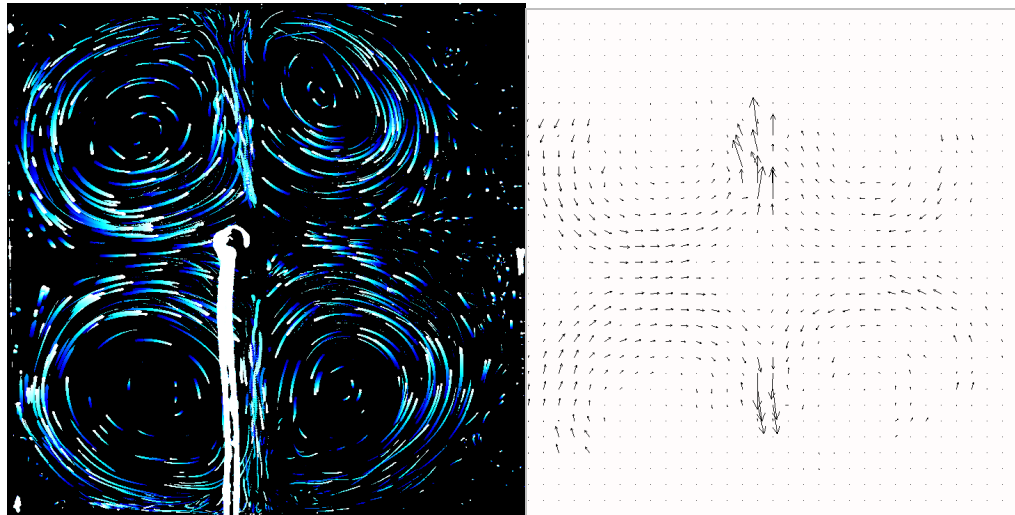


Figure 2.3: Path lines and grid velocity vectors created by Pliolite particles

2.2 Numerical methods

The computational fluid dynamics (CFD) simulations by FLUENT 6.3.26 were subsequently carried out to analyze the flow in the plenum. The physical properties of flow are important for the heat transfer near a wall, so more accurate heat transfer study can be achieved through CFD simulations than a 1D model because it enables us to analyze the flow thermally and spatially. CFD simulations also enable us to change the geometry of model very easily, so it is helpful for case studies. As remarked in the Chapter 1, we consider several independent parameters such as flow rate, plenum depth, inlet area, inlet position, and gravity. The case studies with those parameters were performed and investigated using FLUENT.

The geometry of the computational domain was identical to that of the experimental setting as shown in Figure 2.4, but a real scale is used. In the experiment, four symmetric vortexes are produced. Utilizing symmetrical boundary conditions only one-quarter of the plenum was modeled in order to save computational cost, and no entrainment is assumed between the vortices.

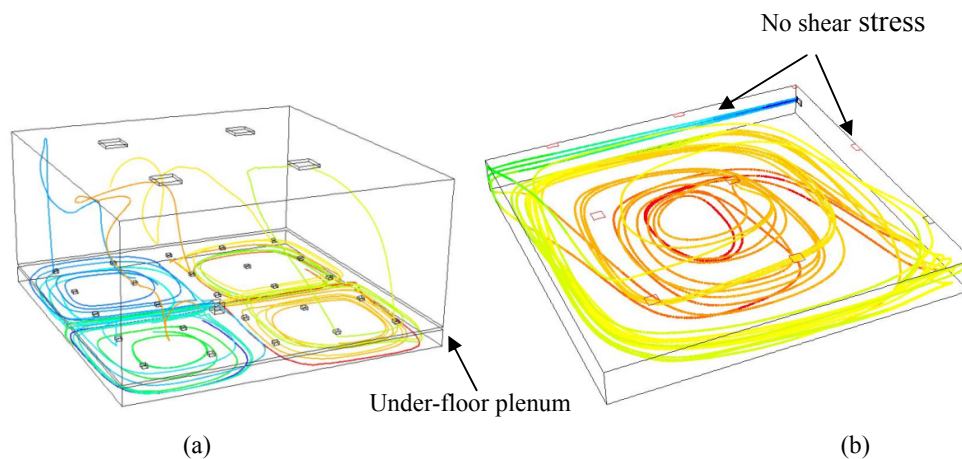


Figure 2.4: An Under-floor plenum in a typical room (a) and one-quarter plenum for computational domain (b)

The plenum model considers only one quarter of the entire plenum, and the number of inlet and diffusers are decreased to 1 and 9, respectively. No shear-stresses boundary conditions are applied on the walls where vortices were supposed to be in contact each other. Another plenum geometry used in the investigation of inlet area and position variations will be described in that Chapter 4 and 5. The volume was filled with tetprimitive elements, and the mesh near to top and bottom walls is more compressed. Isothermal boundary condition of 294K was set on the bottom of the plenum, and the temperature of inlet supply air to the plenum was fixed to 288K in all cases. All walls except bottom plate were assumed to be adiabatic.

In this thesis the Reynolds-averaged Navier-Stokes equations (RANS) based on the renormalization group (RNG) K - ε turbulence model of FLUENT is employed. The RNG K - ε model is derived from the Navier-Stokes equations using a statistical technique called renormalization group theory. This turbulence model is widely used for simulating indoor airflows due to its stable performance (Zhang *et al.*, 2007).

To derive the k equation we start with Navier-Stokes equations,

$$\frac{D}{Dt}u_i = -\frac{1}{\rho}\nabla P + \nu\nabla^2u_i \quad (\text{Equation 2.1})$$

With Reynolds decomposition and ensemble averaging, the Reynolds equations for mean velocity is

$$\frac{\overline{D}}{\overline{Dt}}\overline{u}_i = -\frac{1}{\rho}\frac{\partial\overline{P}}{\partial x_i} + \nu\nabla^2\overline{u}_i - \frac{\partial}{\partial x_j}\overline{u_i u_j} \quad (\text{Equation 2.2})$$

, where the overbar represents the ensemble average and the dash implies a fluctuation. By subtracting the Reynolds equations from the Navier-Stokes equations, the fluctuating velocity evolve by

$$\frac{D}{Dt} u_i' = -\frac{1}{\rho} \frac{\partial \bar{P}}{\partial x_i} + \nu \nabla^2 \bar{u}_i - u_j' \frac{\partial}{\partial x_j} \bar{u}_i + \frac{\partial}{\partial x_j} \overline{u_i' u_j'} \quad (\text{Equation 2.3})$$

From Equation 3 the transport equation for turbulent kinetic energy k , is derived as

$$\frac{\partial k}{\partial t} + \overline{u_j} \frac{\partial k}{\partial x_j} + \frac{\partial}{\partial x_j} \frac{1}{2} \overline{u_i' u_i' u_j'} + \frac{1}{\rho} \frac{\partial \overline{u_i' P'}}{\partial x_i} - 2\nu \frac{\partial}{\partial x_j} \overline{u_i' S_{ij}'} = -\overline{u_i' u_j'} \frac{\partial}{\partial x_j} \bar{u}_i - 2\nu \overline{S_{ij}' S_{ij}'} \quad (\text{Equation 2.4})$$

This equation can be simplified to

$$\frac{D}{Dt} k + \nabla \cdot T_j' = P - \varepsilon \quad (\text{Equation 2.5})$$

$$\text{, where } T_j' = \frac{1}{2} \overline{u_i' u_i' u_j'} + \frac{1}{\rho} \overline{u_i' P'} - 2\nu \overline{u_i' S_{ij}'}, \quad P = -\overline{u_i' u_j'} \frac{\partial}{\partial x_j} \bar{u}_i$$

The gradient-diffusion hypothesis (Equation 2.6) is used to model the second term in the left hand side as

$$\langle u \phi' \rangle = -\Gamma_T \nabla \langle \phi \rangle \quad (\text{Equation 2.6})$$

, where $\langle u \phi' \rangle$: scalar flux , $-\nabla \langle \phi \rangle$: mean scalar gradient , and $-\Gamma_T$: turbulent diffusivity

Thus, the second term in Equation 2.5 becomes

$$T_j' = -\frac{\nu_T}{\sigma_k} \nabla k \quad \text{, where } \sigma_k = \text{turbulent Prandtl number for } k \quad (\text{Equation 2.7})$$

In Equation 2.7 the eddy viscosity is defined by

$$\nu_T = C_\mu \frac{k^2}{\varepsilon} \quad (\text{Equation 2.8})$$

Lastly, the k equation becomes

$$\frac{\overline{D}}{Dt} k = \nabla \cdot \left(\frac{v_T}{\sigma_k} \nabla k \right) + P - \varepsilon \quad (\text{Equation 2.9})$$

Now consider the equation for turbulent dissipation ε . We assume that it can be modeled similarly to the k equation (Equation 2.9).

$$\frac{\overline{D}}{Dt} \varepsilon = \nabla \cdot \left(\frac{v_T}{\sigma_\varepsilon} \nabla \varepsilon \right) + C_{\varepsilon 1} \frac{P\varepsilon}{k} - C_{\varepsilon 2} \frac{P\varepsilon^2}{k} + R_\varepsilon \quad (\text{Equation 2.10})$$

For the standard K - ε model the unknown constants such as C_μ , $C_{\varepsilon 1}$, and $C_{\varepsilon 2}$, can be obtained empirically, but for the RNG K - ε model the constants are derived analytically by the RNG theory and take the values (Choudhury, 1993).

$$C_\mu = 0.0845, \quad C_{\varepsilon 1} = 1.42, \quad \text{and} \quad C_{\varepsilon 2} = 1.68 \quad (\text{Equation 2.11})$$

The RNG K - ε model has R term that does not show up in standard K - ε model, and it significantly improves its accuracy for rapidly strained flows.

$$R_\varepsilon = \frac{C_\mu \rho \eta^3 (1 - \eta / \eta_o) \varepsilon^2}{1 + \beta \eta^3} \frac{1}{k} \quad (\text{Equation 2.12})$$

, where $\eta \equiv Sk / \varepsilon$, $\eta_o = 4.38$, and $\beta = 0.012$

In Chapter 6 the effect of buoyancy will be investigated. When the Boussinesq approximation for density is applied, the buoyancy term derived from Navier-Stokes equation becomes

$$G_b = \beta g_i \langle T_i u_i' \rangle \quad (\text{Equation 2.13})$$

Then the buoyancy term is modeled via eddy diffusivity.

$$G_b = \beta g_i \frac{\mu_t}{Pr_t} \frac{\partial T}{\partial x_i} \quad (\text{Equation 2.14})$$

This buoyancy term should be added to the equation when the effect of buoyancy is considered.

The SIMPLE algorithm for resolving the coupling between pressure and velocity was employed. When the buoyancy is on the PRESTO! scheme is used as a pressure interpolation scheme.

3 THE EFFECT OF FLOW RATE AND PLENUM DEPTH

3.1 Observations

The objective of this chapter is to observe the physical behaviors of flow in a plenum as a function of two independent parameters the flow rate Q and plenum depth H . Because we fixed the temperature of inlet air at 288K, the flow rate directly related to the cooling load from a chiller. The residence time and path length are calculated along with residence time probability distributions. The average Reynolds number \overline{Re} of flow in the plenum and average Nusselt number \overline{Nu} on the lower surface area are calculated, and the change of the standard deviations (STD) of air temperatures at the diffusers with plenum depth and flow rate is also obtained.

For the computational efficiency, only one-quarter of the plenum $2.89 \times 2.89 \times H$ was simulated. The particles were injected from an inlet, but we inversely track the trajectories of 338 imaginary air particles from diffusers to an inlet in order for all diffusers to have the same flow rate.

Fig.3.1 shows the particle paths generated by air particles and the changes of flow patterns with flow rates and plenum depths. When the plenum depth $H=0.2\text{m}$, the vortex pattern show two-dimensional motion, and does not change with flow rate significantly. However, three-dimensional motions are detected with increasing flow rate when the plenum depth becomes deeper.

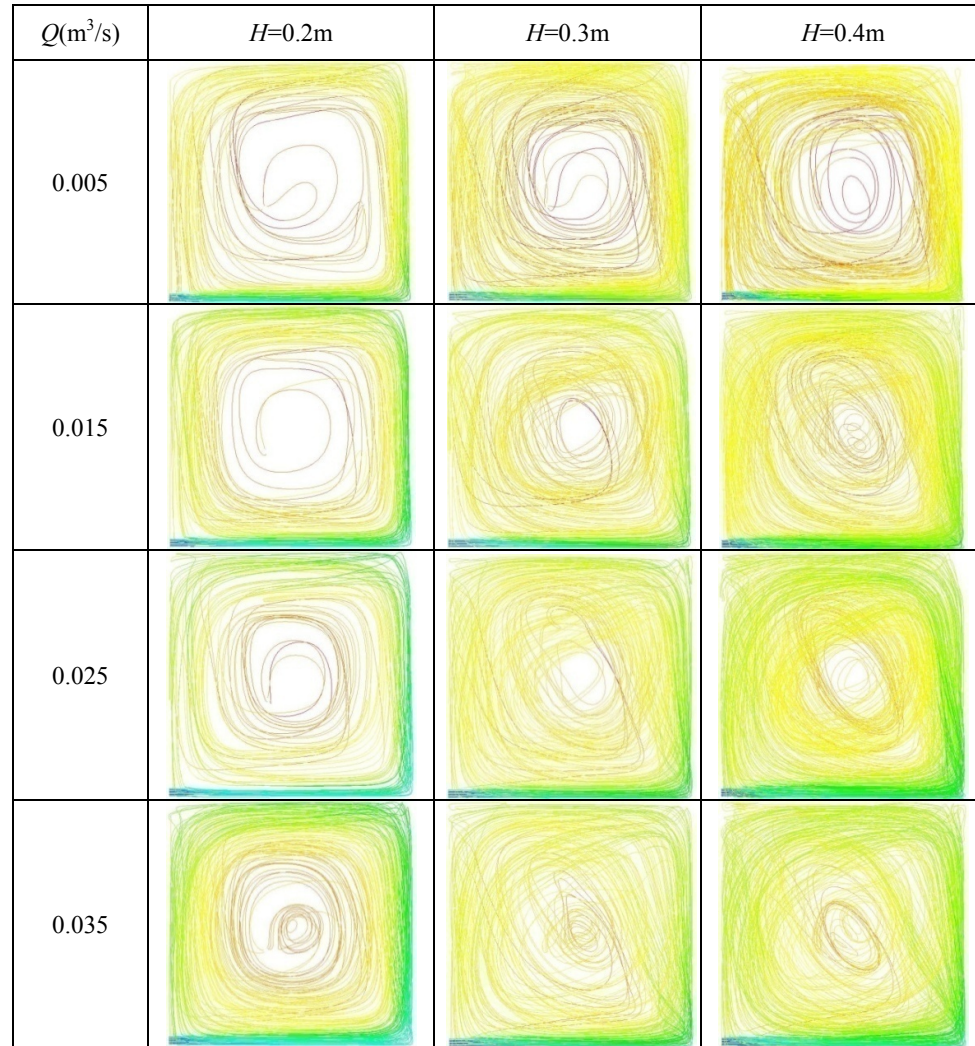


Figure 3.1: The flow patterns corresponding to the flow rates and plenum depths

After the individual residence time of each particle was measured, the residence time distribution was produced. It was observed that the shape of the distribution was very similar to that of gamma distribution, so we created the gamma probability density function (PDF) of residence times of 338 air particles by a gamma curve-fitting tool of Matlab. For large random samples, the distribution of the data typically reflects the original property of the population, and we found the property was not clear when we use less than 200 sample particles. Due to limited

time, we used no more than 338 sample particles to obtain the distributions. With this number of particles we observed the variability of the population as shown in Figure 3.2. The distribution is broadened when the plenum depth increases, and the population is more condensed near to the origin when the flow rate is increased.

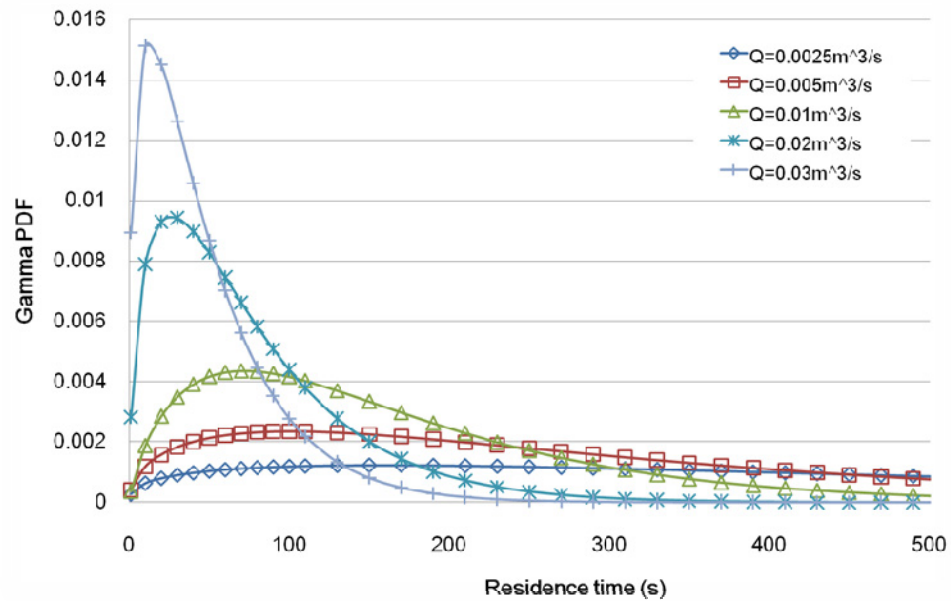


Figure 3.2: Residence time distribution corresponding to flow rate ($H=0.2\text{m}$)

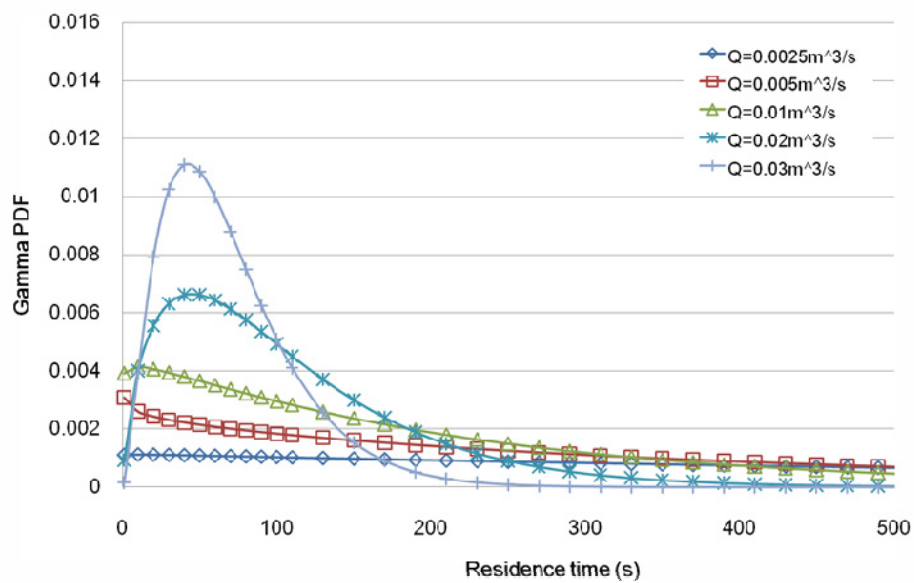


Figure 3.3: Residence time distribution corresponding to flow rate ($H=0.3\text{m}$)

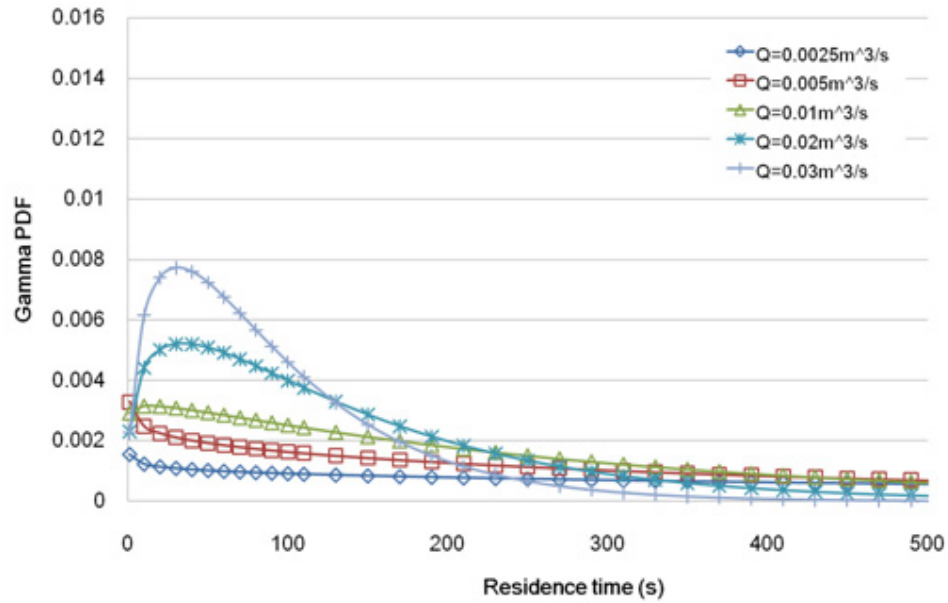


Figure 3.4: Residence time distribution corresponding to flow rate ($H=0.4\text{m}$)

Typically, the gamma distribution is defined in terms of scale and shape factors that are automatically generated by Matlab. Based on the scale and shape factors, the average residence time of 338 air particles was calculated. As the flow rate increased, the average residence time also increased. The change of average residence time with flow rate and plenum depth is shown in Figure 3.5, and Equation 3.1 can formulate their correlation corresponding to the plenum depths.

$$t = \frac{c}{Q} \quad (\text{Equation 3.1})$$

, where $c=1.34$ ($H=0.2\text{m}$), $c=2.01$ ($H=0.3\text{m}$), and $c=2.84$ ($H=0.4\text{m}$).

The constant c can be related with the volume of the plenum by Equation 3.2 because the plenum depth H is linearly related to the volume of a plenum $V=H \times L^2$ when a plenum width L is fixed.

$$c = 0.9V \quad (\text{Equation 3.2})$$

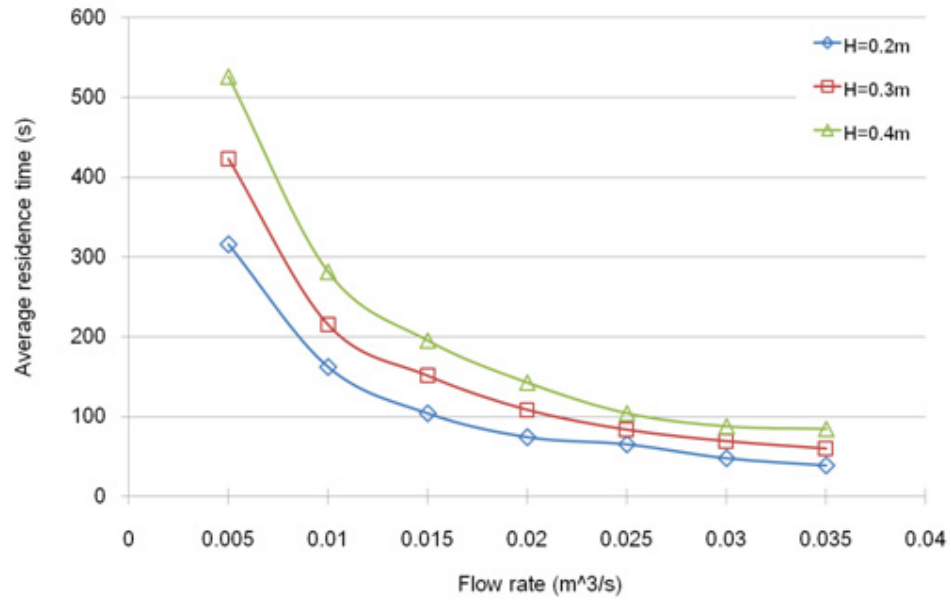


Figure 3.5: The dependence of average residence time on flow rate

The average residence time linearly increases with a plenum depth as shown

Figure 3.6.

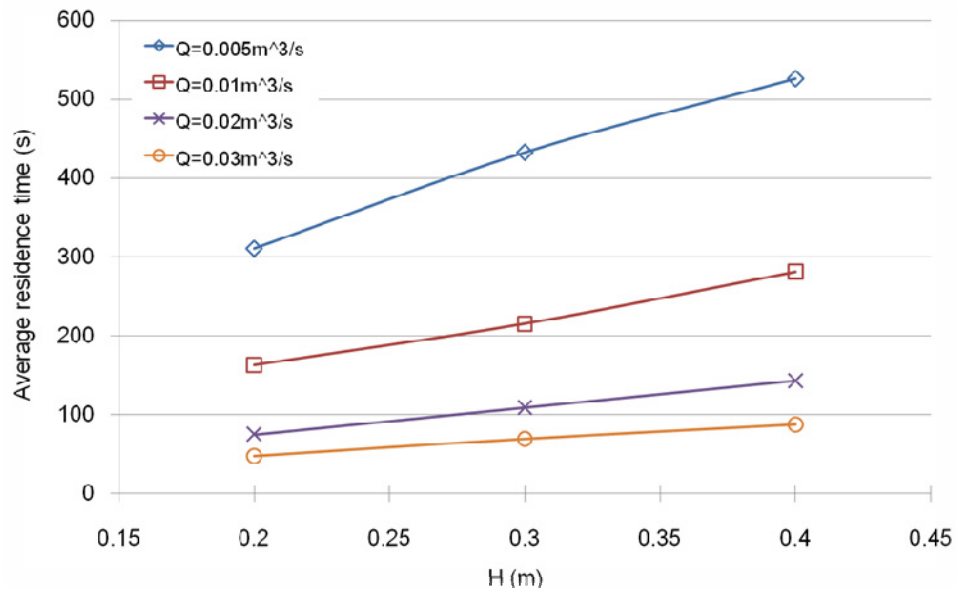


Figure 3.6: The dependence of average residence time with plenum depth

Because the plenum width L is fixed to 2.89m, the volume $V=H \times L^2$ of the plenum is proportional to H . As we checked in Figure 3.5 and 3.6 the average residence time t changes with Q , V , H , and L . Now we may derive two dimensionless groups: the dimensionless residence time $t/(V/Q)$ and the aspect ratio H/L . Equation 3.3 formulates the correlation between the two dimensionless groups.

$$t_r = \frac{t}{V/Q} = f(H/L) \quad (\text{Equation 3.3})$$

From the Equation 3.1 and 3.2 the residence time t is given by

$$t = \frac{0.9V}{Q} \quad (\text{Equation 3.4})$$

If we substitute t in Equation 3.3 by t in Equation 3.4, the dimensionless residence time t_r is found to be 0.9, and the t_r does not change with aspect ratio as shown in Figure 3.7. The average path length increases with flow rate and plenum depth as shown in Figure 3.8.

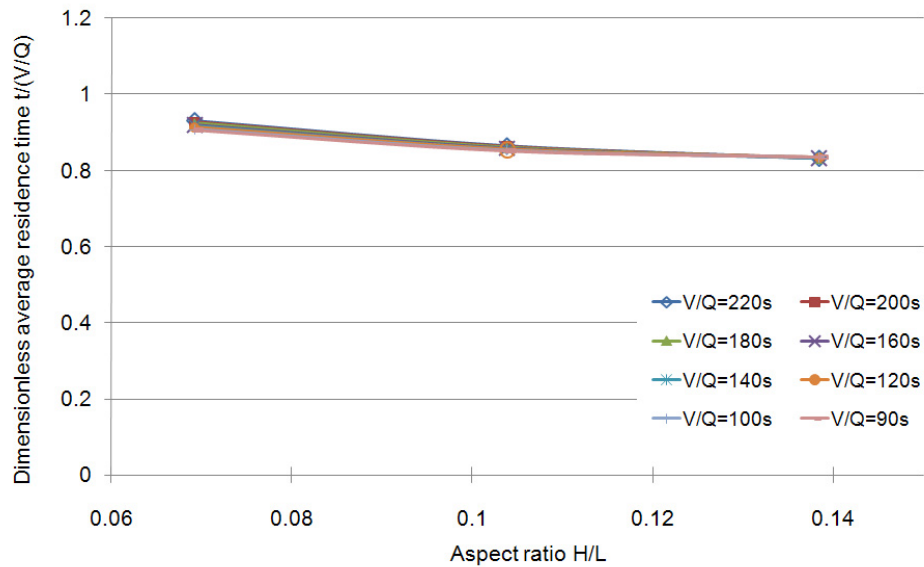


Figure 3.7: The dependence of dimensionless average residence time on aspect ratio

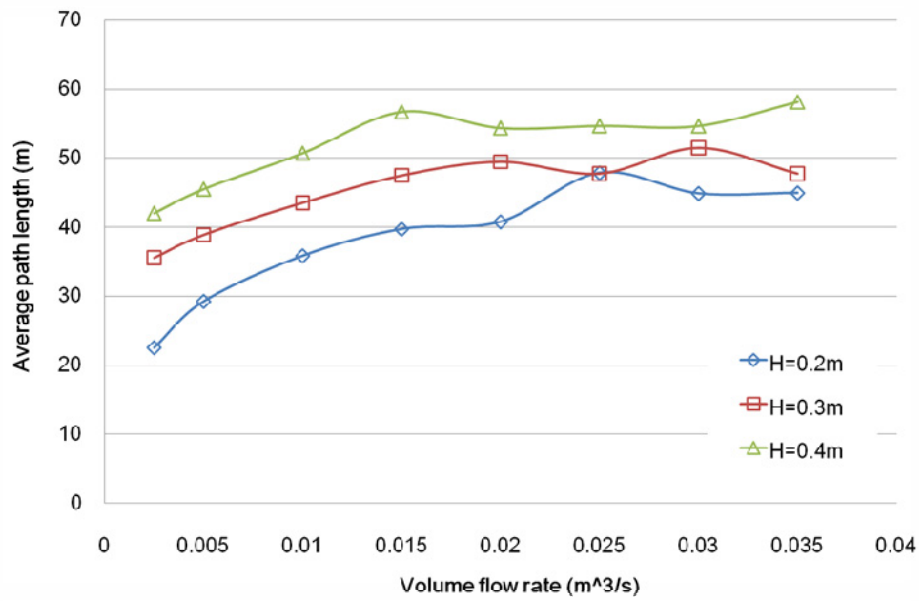


Figure 3.8: Average path length corresponding to flow rates and plenum depths

Based on the average residence times and path lengths measured above, the average velocities of air particles were calculated. These measured average velocities are indicated with solid lines in Figure 3.9. We also show the measured average velocities compared with volume-averaged velocity directly obtained by the FLUENT simulations (dashed lines) in Figure 3.9. The two kinds of average velocities are found to be almost the same. For the average Reynolds number \overline{Re} we select the volume-averaged velocity as a characteristic velocity.

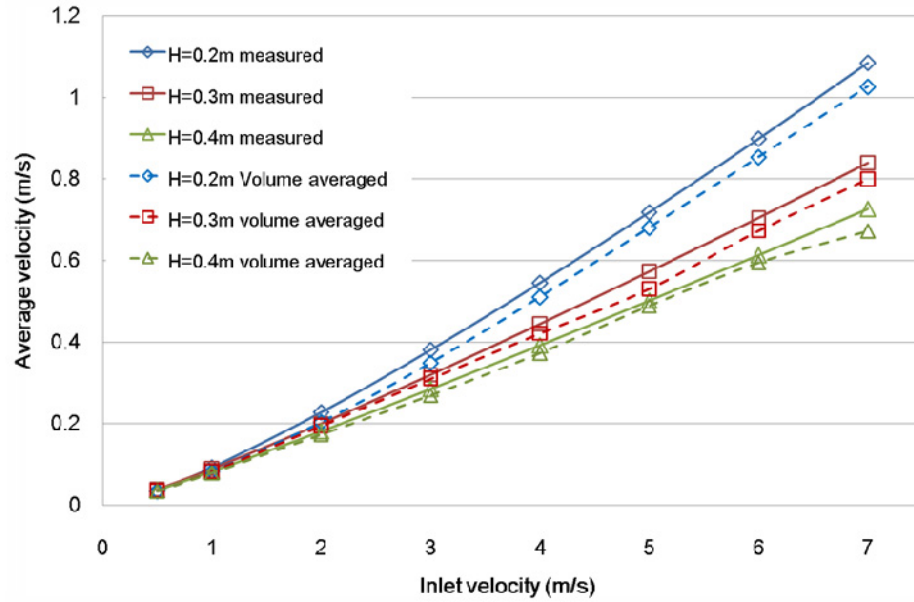


Figure 3.9: Comparison between volume averaged velocities and average velocities calculated from average residence time and path length

The average Nusselt number \overline{Nu} on the bottom surface area is calculated by FLUENT. The solid lines in Figure 3.10 visualize the correlation between \overline{Nu} and \overline{Re} corresponding to plenum depths. Equation 3.5 approximately formulates the correlation, and the approximations are shown as dashed lines in Figure 3.10.

$$\overline{Nu} = c\overline{Re}^{3/4} \quad (\text{Equation 3.5})$$

, where $c=0.088(H=0.2\text{m})$, $c=0.073(H=0.3\text{m})$, and $c=0.062(H=0.4\text{m})$.

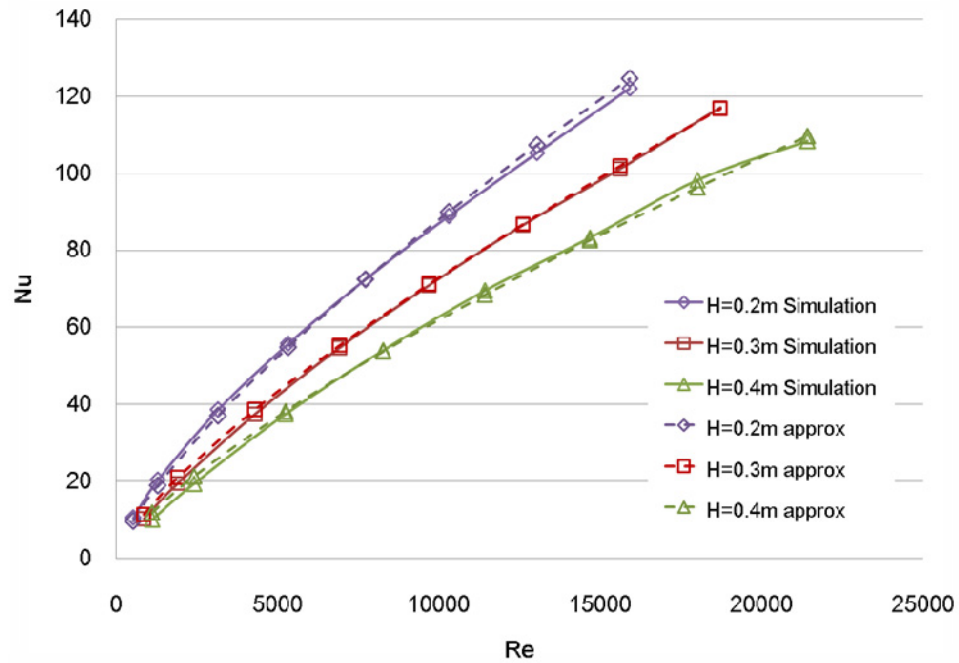


Figure 3.10: The change of \overline{Nu} corresponding to \overline{Re}

The STD of air temperatures at diffusers decreases when the plenum depth is increased, and the flow rate has little effect on STD of outlet temperatures as shown in Figure 3.11. Figure 3.12 shows that the temperature difference dT between the maximum and minimum temperatures at different diffusers decreases as H increases. The flow rate does not affect dT because both the maximum and minimum temperatures decrease together when the flow rate is increased.

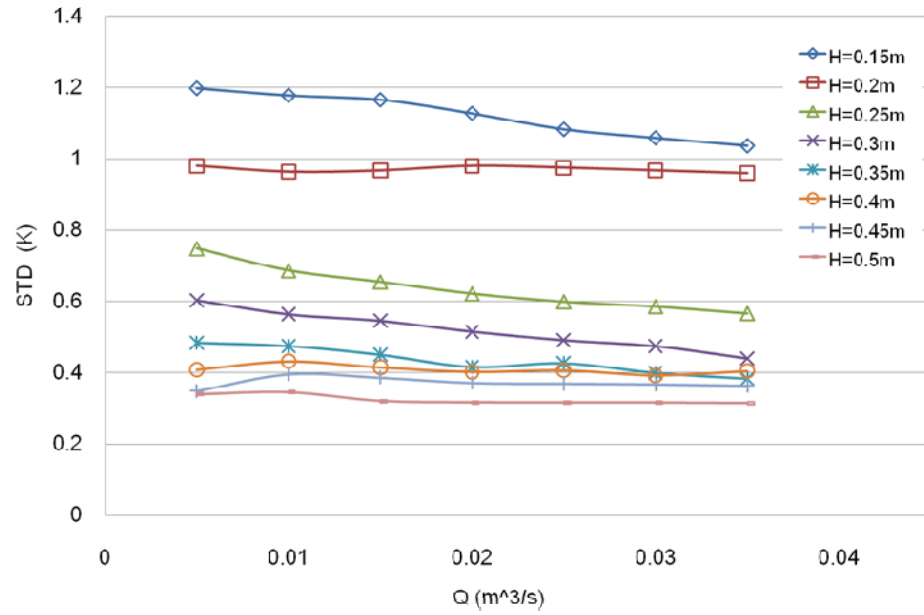


Figure 3.11: The dependence of STD of outlet temperature on plenum depth H and flow rate Q

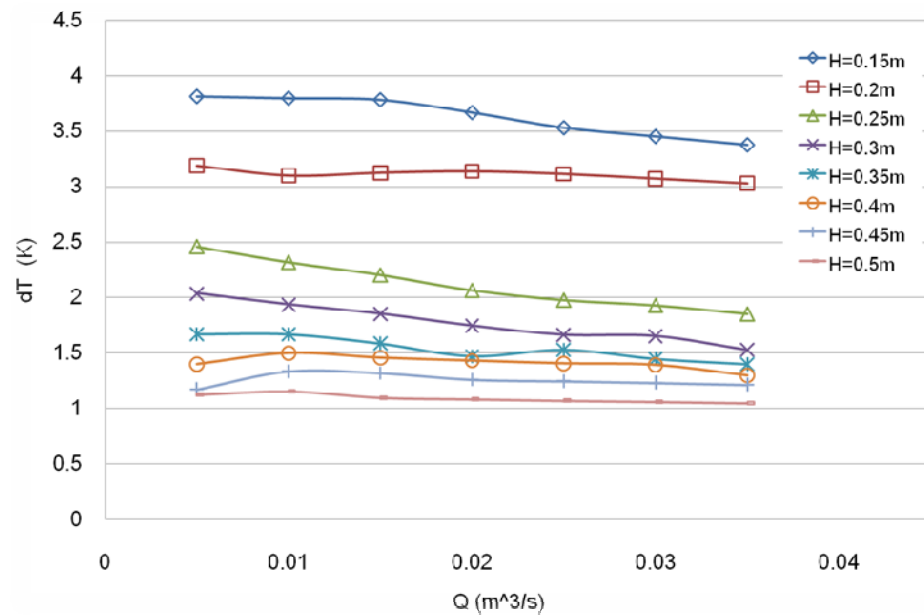


Figure 3.12: The dependence of temperature difference between maximum and minimum air temperature among diffusers on plenum depth and flow rate

3.2 Summary and Discussions

In this Chapter we have observed the physical movements of flow in a plenum. For the plenum of $2.89 \times 2.89 \times H$ m the vortex flow pattern is not really changed with plenum depth and flow rate, but small distortions are detected as shown in Figure 3.1. We observed that the average residence time increased with the volume of a plenum and decreased with flow rate as shown in Figures 3.5 and 3.6. In addition, we observed that the average residence time t is very close to a replenishment time $\tau = V/Q$, therefore the dimensionless residence time $t_r = t/\tau$ becomes close to one as shown in figure 3.7. The limited number of air particles may cause the difference between the two time scales. The \overline{Nu} is observed to increase with \overline{Re} by a power law with the exponent of 0.75 as formulated at Equation 3.5.

We observed that when the flow rate is fixed, the STD of air temperatures leaving diffusers reduced by increasing the plenum depth as shown in Figure 3.12, which may be explained by the behaviors of the residence time distribution. When we fix the flow rate to $0.035 \text{ m}^3/\text{s}$, the different residence time distributions are created by different plenum depths as shown in Figure 3.13. If we design the plenum deeper, the replenishment time marked with the circle is increased, and the residence time distribution becomes more spreaded.

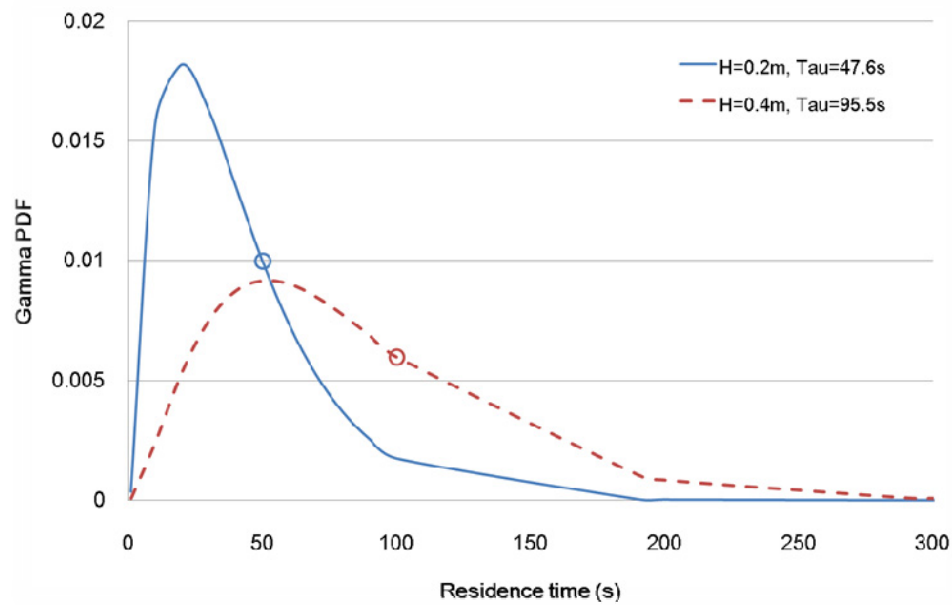


Figure 3.13: Different residence time distributions caused by different plenum depths ($Q=0.035\text{m}^3/\text{s}$)

For the case of deeper plenum the residence time is more evenly distributed through the whole range, so there exist more particles which experience longer residence times than those for shallow plenum. As the fraction of particles having longer residence time is increased, the properties of population may affect on the properties of entire flow. It is difficult to characterize the thermal property of the population with the average temperature of 370 air particles as given in Figure 3.14. However, in Figure 3.15 we may identify the thermal property of the population especially particles that resided longer than $t_r=1$. The STD of temperatures of particles remained in a plenum decreases with time as the trendline formed by the second order polynomial represents. Therefore, the STD of air temperature leaving diffusers may be lower when the plenum becomes deeper because there are more particles with lower temperature variations

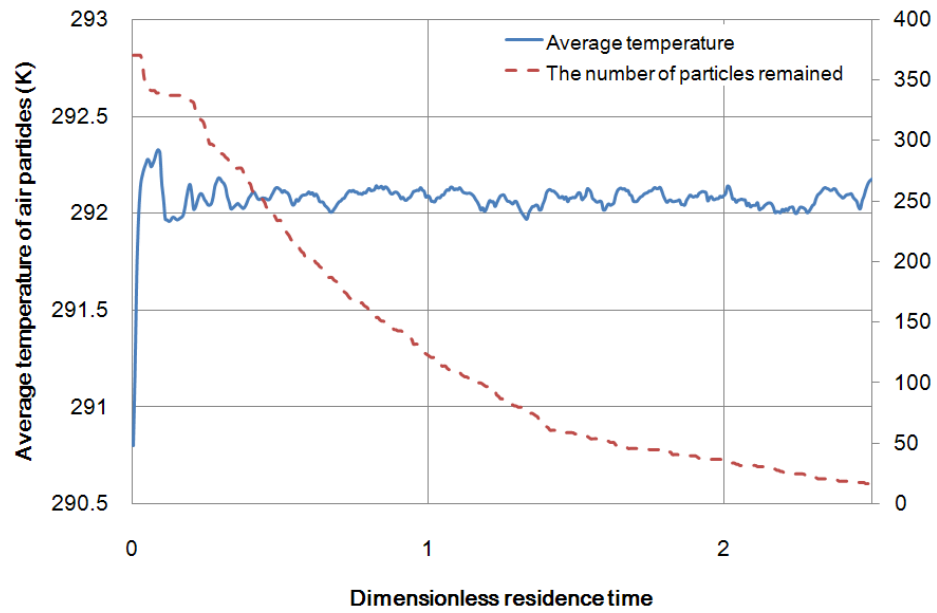


Figure 3.14: The change of average temperature of 370 air particles with dimensionless residence time. Right axis indicates the number of air particles remained in a plenum. ($H=0.4\text{m}$ and $Q=0.02\text{m}^3/\text{s}$)

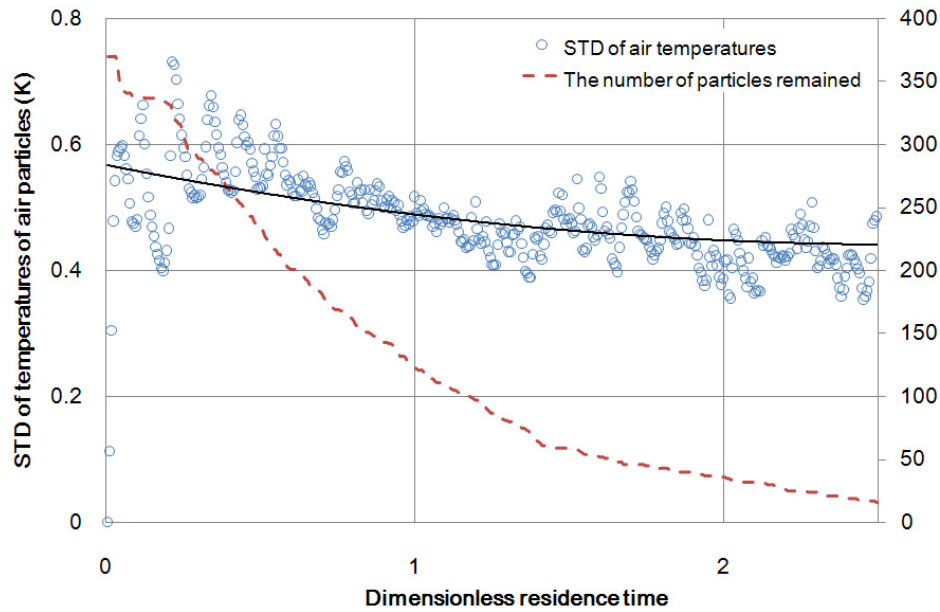


Figure 3.15: The change of STD of temperatures of 370 air particles with dimensionless residence time. Right axis indicates the number of air particles remained in a plenum. ($H=0.4\text{m}$ and $Q=0.02\text{m}^3/\text{s}$)

4 THE EFFECT OF INLET AREA VARIATION

4.1 Observations

The objective of this chapter is to investigate the behaviors of temperature variation through diffusers and heat transfer across a slab corresponding to the change of inlet area. The plenum configuration of $3 \times 6 \times 0.3\text{m}$ is used to observe the effect of inlet area on various dependent parameters such as residence time, path length, STD of outlet temperatures, and heat transfer across a slab.

Figure 4.1 introduces the geometry of plenum used in this chapter which has 20 inlets and 72 diffusers. We built a number of inlets to give a flexibility to control inlet configuration. The area of a single inlet was 0.01m^2 , and the total inlet area was varied by controlling the number of open inlets. The flow rate is fixed to $0.02\text{m}^3/\text{s}$ which is equivalent to replenishment time of 270s for all cases. The temperatures of inflow and bottom surface were fixed at 288K and 294K, respectively.

The seven cases, we call it group A, of inlet configurations corresponding to each case number are described in Figure 4.1.

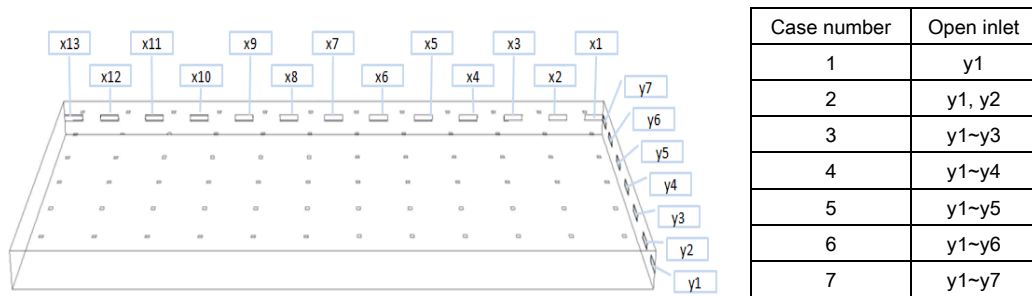


Figure 4.1: Plenum geometry and inlet configurations at each case (group A)

Figure 4.2 shows trajectories and overall flow patterns created by air particles released from the inlets. In the right column, it also shows the \overline{Nu} contours on the bottom surface area, so we can see where the most heat transfer from a slab occurs

for each flow pattern. As the inlet configuration changes the big vortex pattern is gradually minimized, and it disappears at case 6.

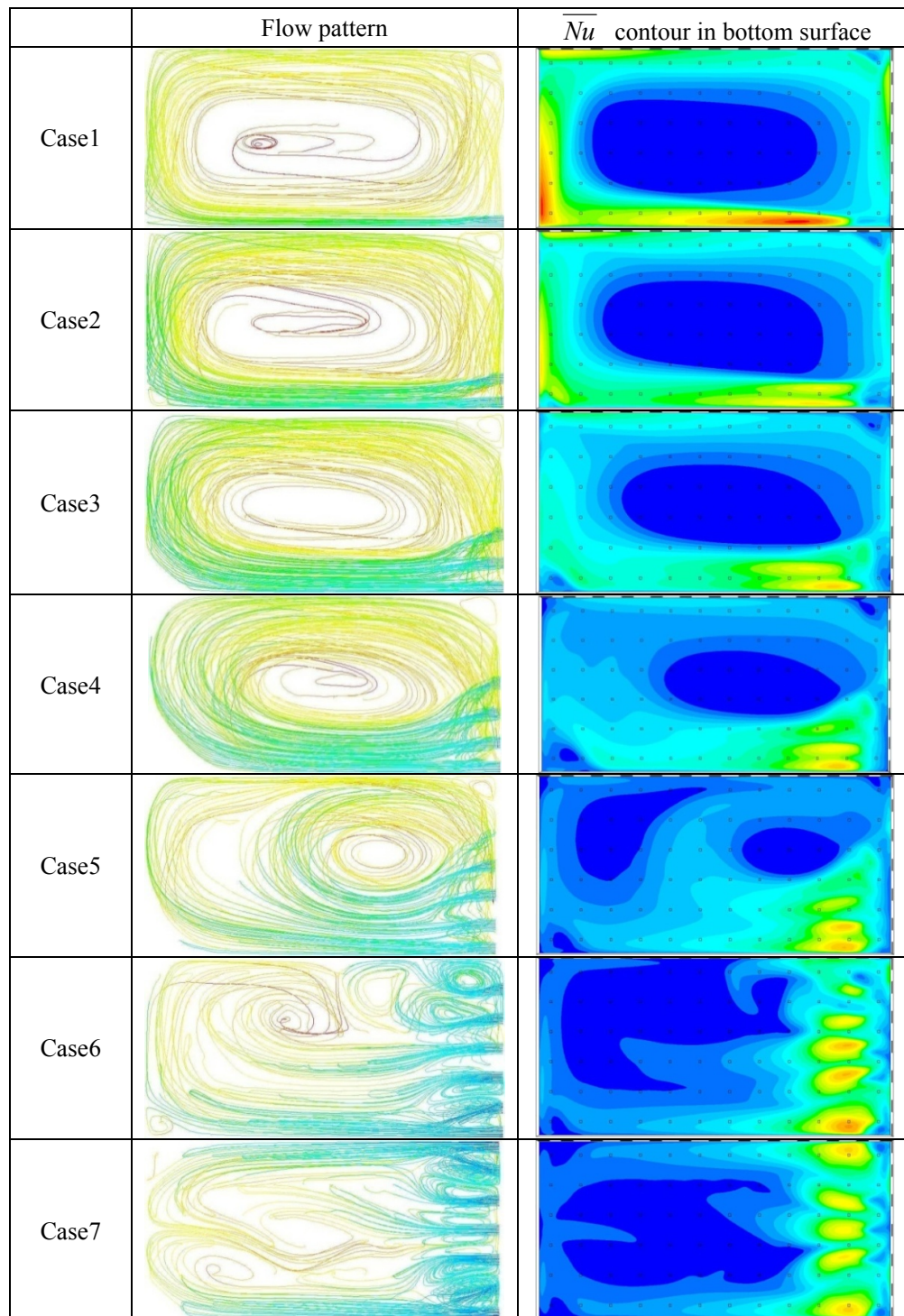


Figure 4.2: The change of flow patterns and \overline{Nu} contours depending on inlet configurations (group A)

The other seven cases, we call it group B, of inlet configurations corresponding to each case number are described in Figure 4.3. The flow rate is fixed to $0.02\text{m}^3/\text{s}$ for all cases.

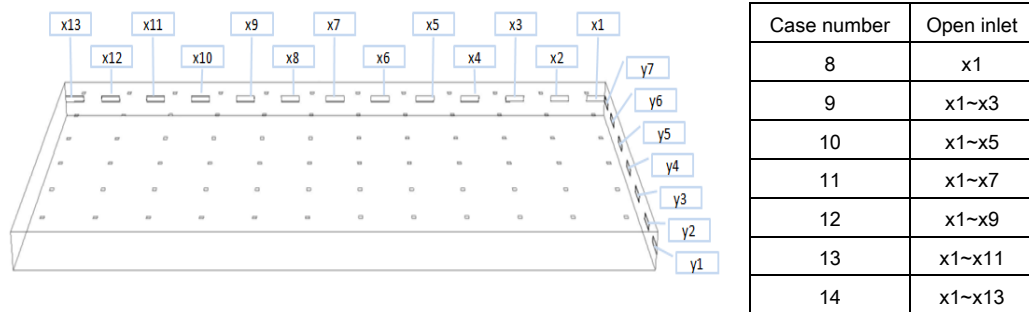


Figure 4.3: Plenum geometry and inlet configurations at each case (group B)

Figure 4.4 shows the change of flow patterns and \overline{Nu} contours for each case in group B. As the inlet configuration changes, the big vortex pattern gradually decreases, and it disappears when it reaches at case 14.

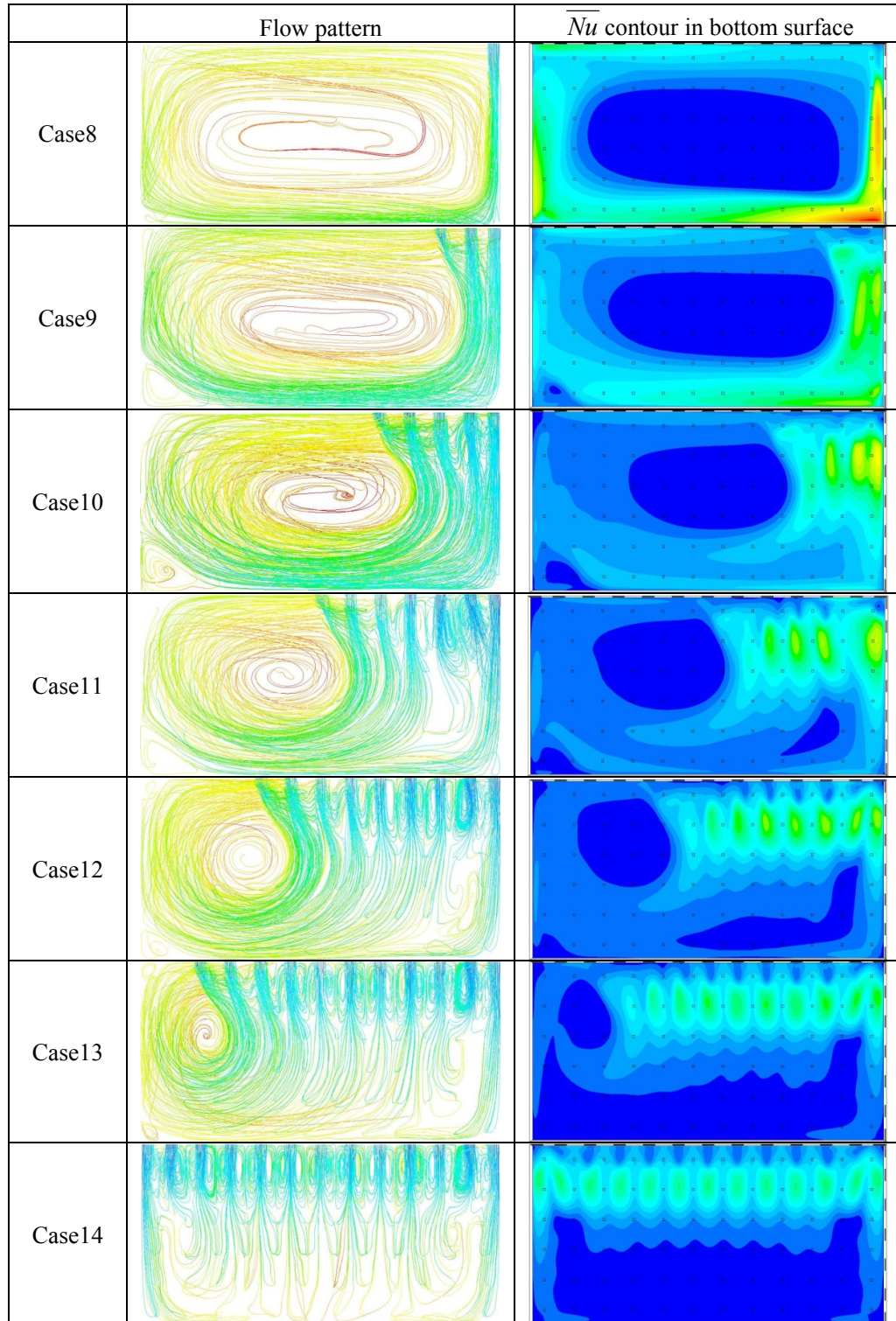


Figure 4.4: The change of flow pattern and \overline{Nu} contour depending on inlet configuration (group B)

Around 576 air particles were released from an inlet in order to measure their average residence times and path lengths. Using the gamma distribution curve fitting, the distributions corresponding to the average residence times are shown in Figures 4.5 and 4.6. The residence time distributions for either group A and B are not changed significantly when the inlet configuration changes.

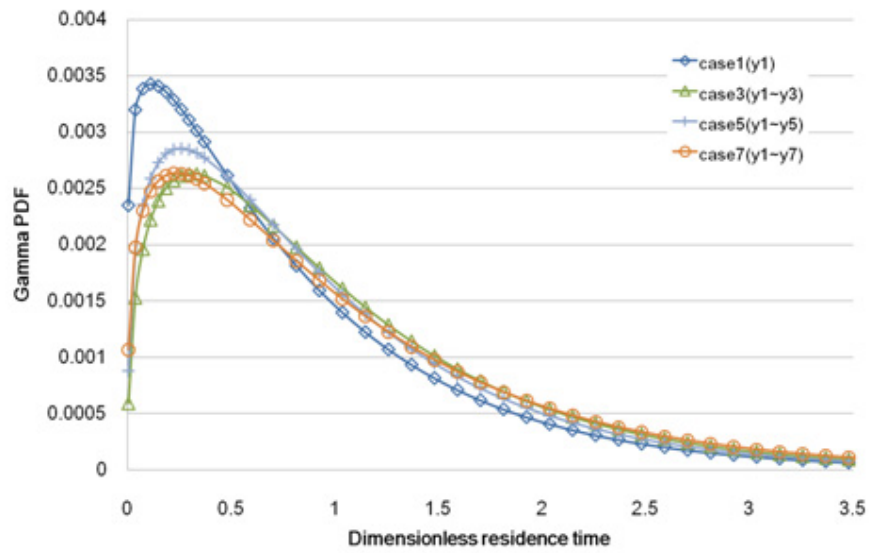


Figure 4.5: Residence time distribution corresponding to inlet configurations (group A)

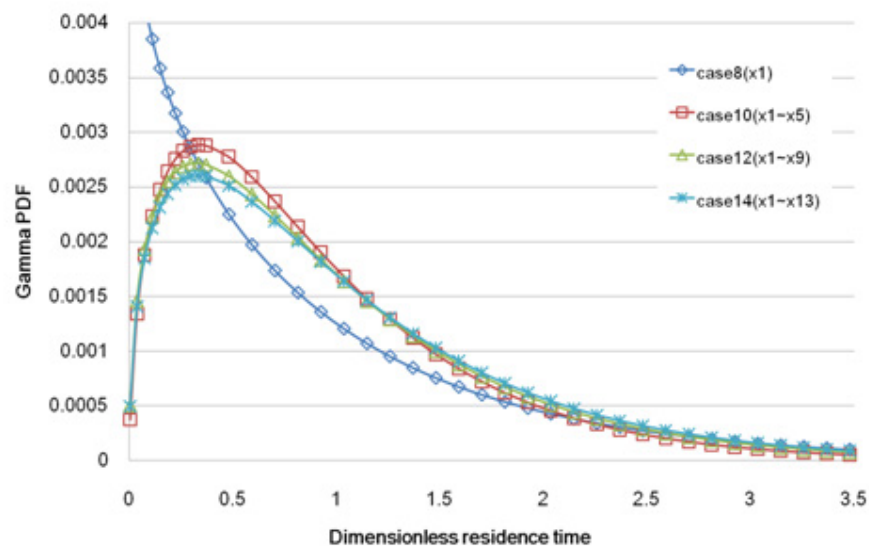


Figure 4.6: Residence time distribution corresponding to inlet configurations (group B)

The average residence time do not change significantly with inlet area, and it remains around 270 s which is the replenishment time.

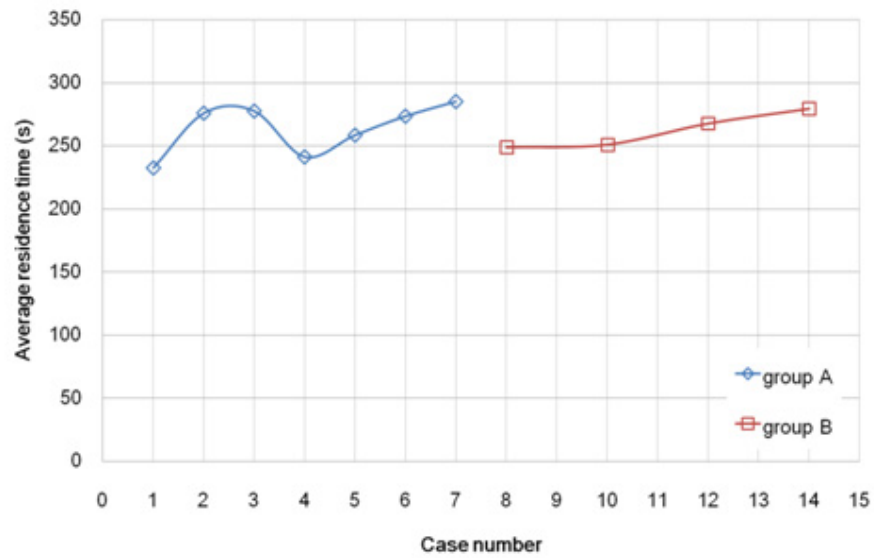


Figure 4.7: Average residence times depending on inlet area ($\tau=270s$)

While the residence time distributions had shown only small changes with inlet area, the path length distributions show considerable changes with inlet area as shown in Figure 4.8 and 4.9. As the inlet area is increased, there is more population gathered near to short path length region.

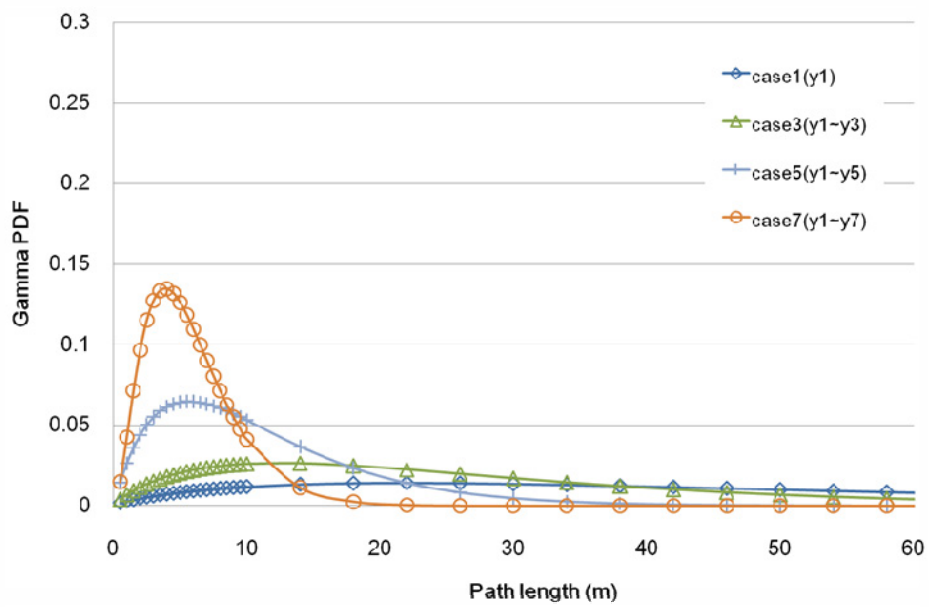


Figure 4.8: Path length distribution corresponding to inlet configurations (group A)

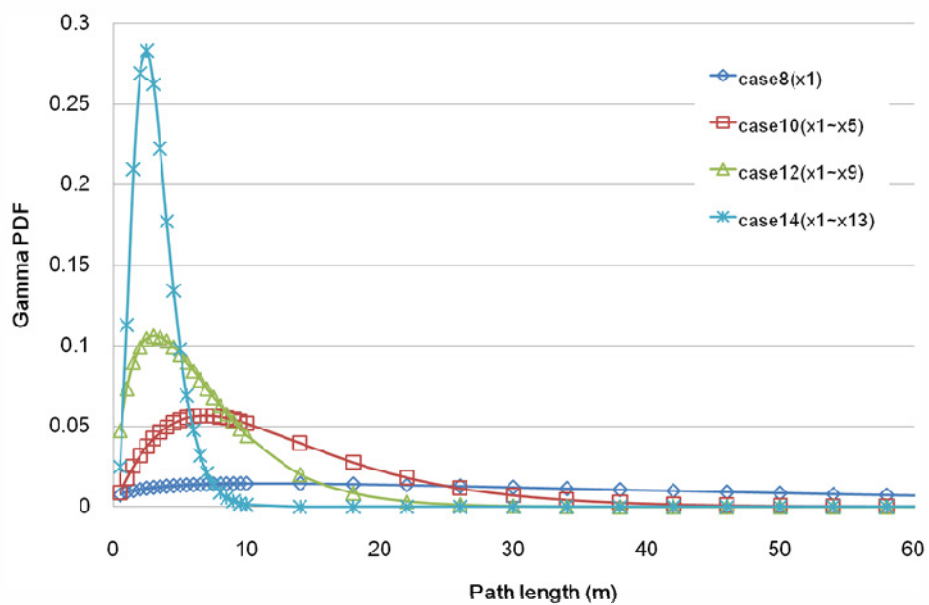


Figure 4.9: Path length distribution corresponding to inlet configurations (group B)

As the inlet area is increased, the average path length decreases as indicated in Figure 4.10. Figure 4.11 shows that the \overline{Nu} on the bottom surface of plenum is decreased when the inlet area is increased, but \overline{Nu} reaches the minimum value before the inlet area becomes the maximum.

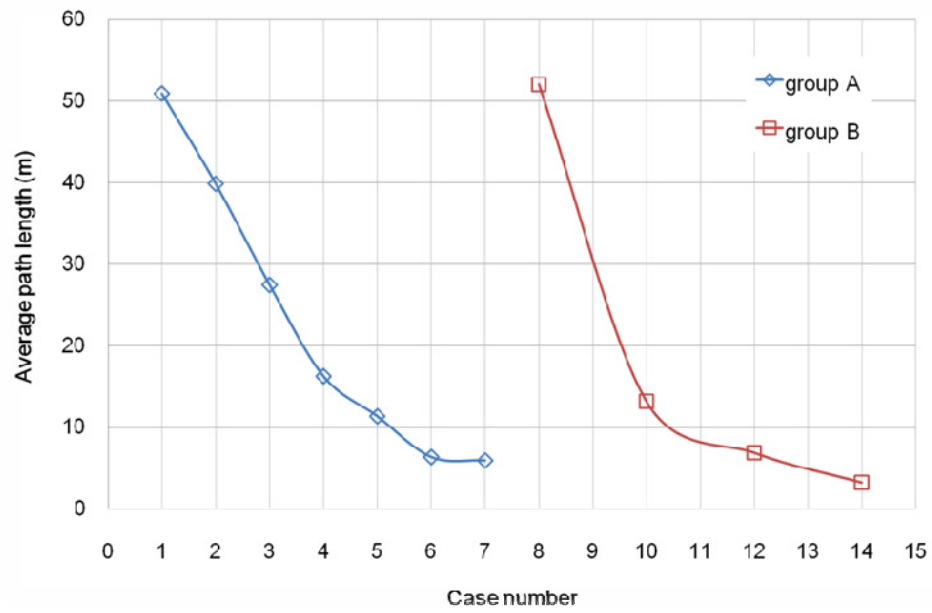


Figure 4.10: Average path lengths depending on inlet area

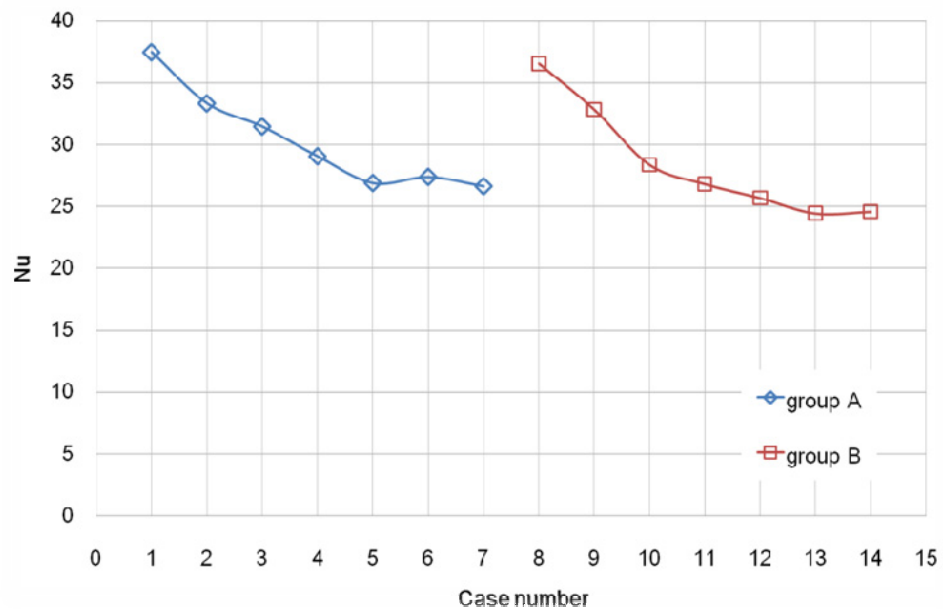


Figure 4.11: Average \overline{Nu} depending on inlet configuration

The STD of air temperatures at diffusers fluctuates with inlet configuration as shown in Figure 4.12. After initial small rise the STD gradually decreases to reach the minimum value, and then it rises again abruptly.

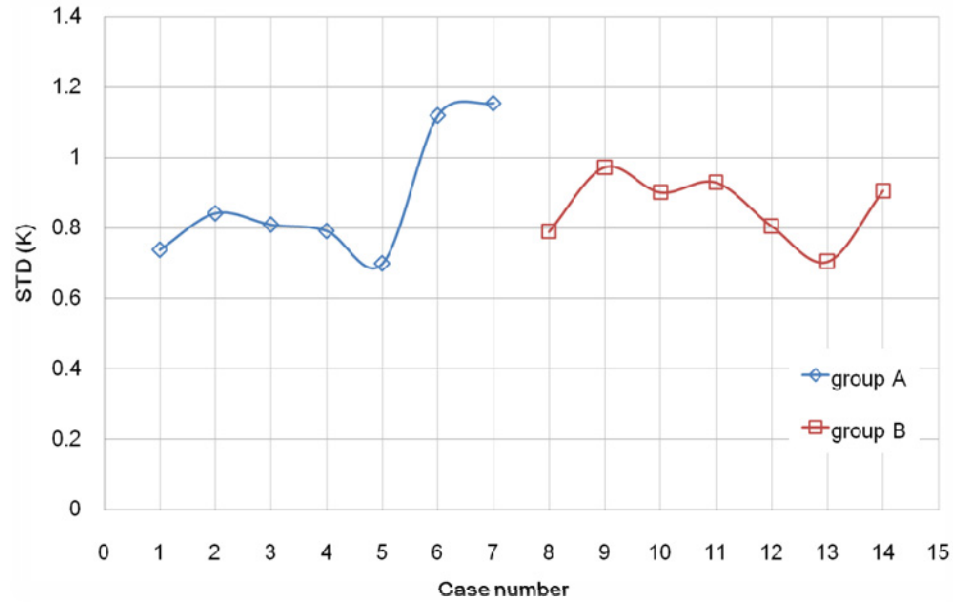


Figure 4.12: STD of outlet temperatures depending on inlet configuration

4.2 Summary and discussions

In this chapter, we have observed how the change of inlet area affects the physical and thermal properties of flow. We enlarged the effective inlet area by increasing number of open inlets. The flow pattern changed as the inlet configuration changed as presented in Figure 4.2 and 4.4. The Nusselt number Nu contours predict the spots where the high heat transfer could occur, so insulation on the surface may avoid critical heat transfer.

When the flow loses a dominant vortex pattern, the STD rises. In Figure 4.12, the STD was observed to increase abruptly for case 6 and 14, and the change of flow pattern may account for this behavior. The change of average temperature of 100 air particles with dimensionless residence time is shown in Figure 4.13. The vortex structure remains in Cases 1, 3, and 5 while it disappears in Case 6. The average temperature of the flow without vortex structure (Case 6) continues to

increase until τ reaches around 1 s, therefore the average temperature difference between two groups of particles whose dimensionless residence time is less than 1 and higher than 1 is bigger than that of Cases 1, 3, and 5 on which the average temperature does not increase with time after around $\tau = 0.4$ s.

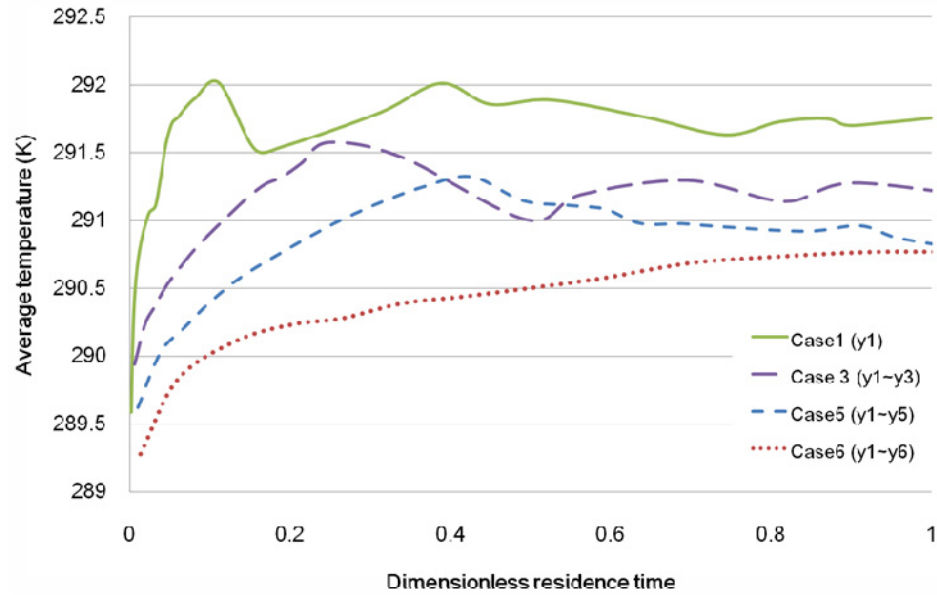


Figure 4.13: The change of average temperature of 100 air particles with dimensionless residence time corresponding to Case 1, 3, 5, and 6. The inlet ID for open inlets are indicated in parenthesis in legend.

The \overline{Nu} decreases when the inlet area increases as shown in Figure 4.11. When the volume averaged-velocity is chosen to be a characteristic velocity for \overline{Re} , the correlation between \overline{Nu} and \overline{Re} is represented in Figure 4.13. When the inlet area increases, the average Reynolds number \overline{Re} decreases along with a decrease of \overline{Nu} .

In Figure 4.14 the data provided in Figure 4.13 are compared to the data obtained from simulations using the plenum of $2.89 \times 2.89 \times 0.3$ m. It may

demonstrate the effect of inlet area and replenishment time on the behaviors of \overline{Nu} and \overline{Re} . The replenishment time is changed by flow rate. With an inlet area of 0.0025m^2 , \overline{Re} and \overline{Nu} are increased to 10000 and 70, respectively, when the replenishment time decreased to 125s (solid arrow). If we enlarge the inlet area to 0.015m^2 , \overline{Nu} and \overline{Re} are decreased to 4500 and 55 correspondingly (dashed arrow), therefore a reduction of \overline{Nu} and \overline{Re} may be achieved by an enlargement of inlet area.

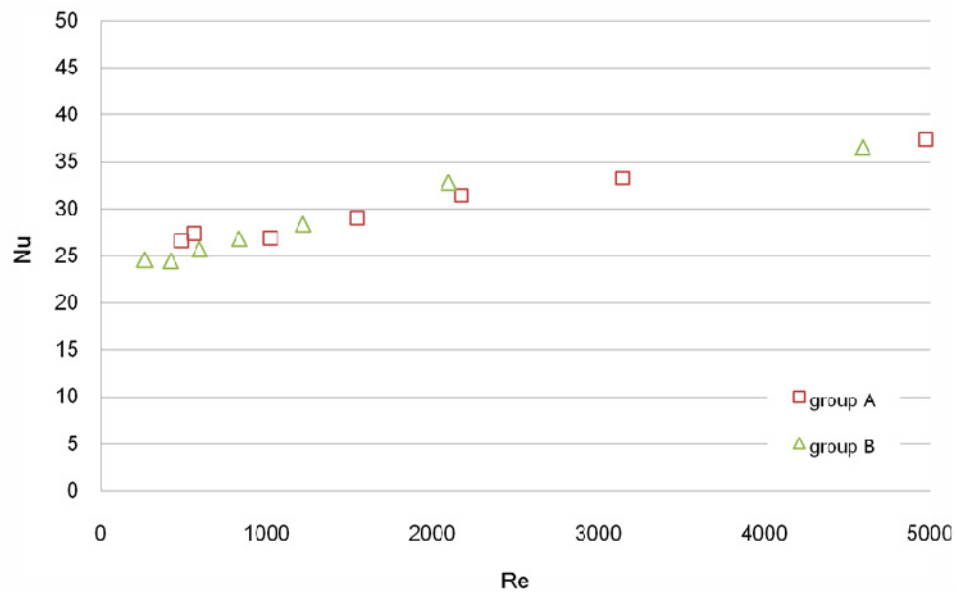


Figure 4.14: The change of \overline{Nu} with \overline{Re} ($\tau=270\text{s}$)

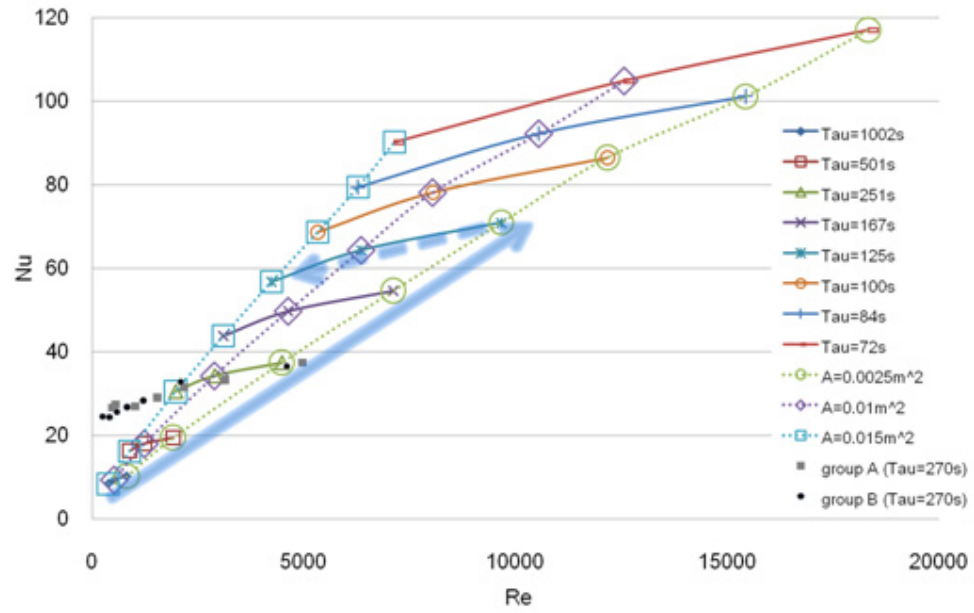


Figure 4.15: The behaviors of \overline{Nu} and \overline{Re} depending on replenishment time and inlet area

5 THE EFFECT OF INLET POSITION

5.1 Observations

The objective of this chapter is to investigate how the heat transfer and STD of outlet temperatures change with inlet position. We vary inlet position from case 1 to case 7, and their positions and case numbers are defined in Figure 5.1. The plenum of $3 \times 6 \times 0.3\text{m}$ was used, and all cases had the same inlet area of 0.01m^2 and flow rate of $0.02\text{m}^3/\text{s}$ which is equivalent to 13.3ACH in the plenum. No buoyancy effect is considered.

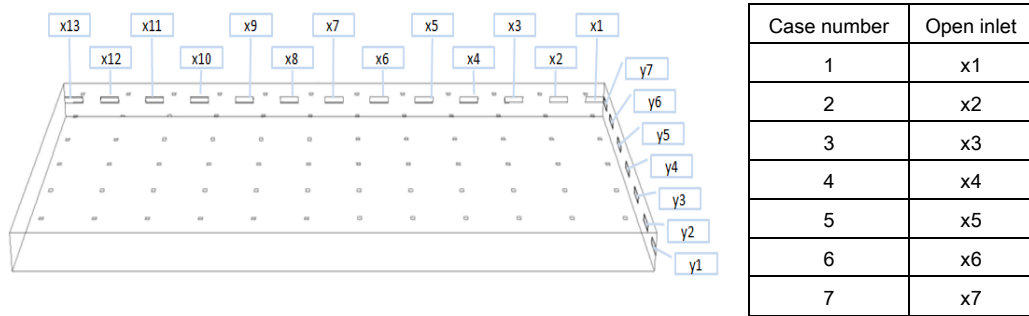


Figure 5.1: Case numbers corresponding to inlet positions

In the Figure 5.2, the flow patterns created by particle paths and \overline{Nu} contours on the bottom surface of all cases are shown.

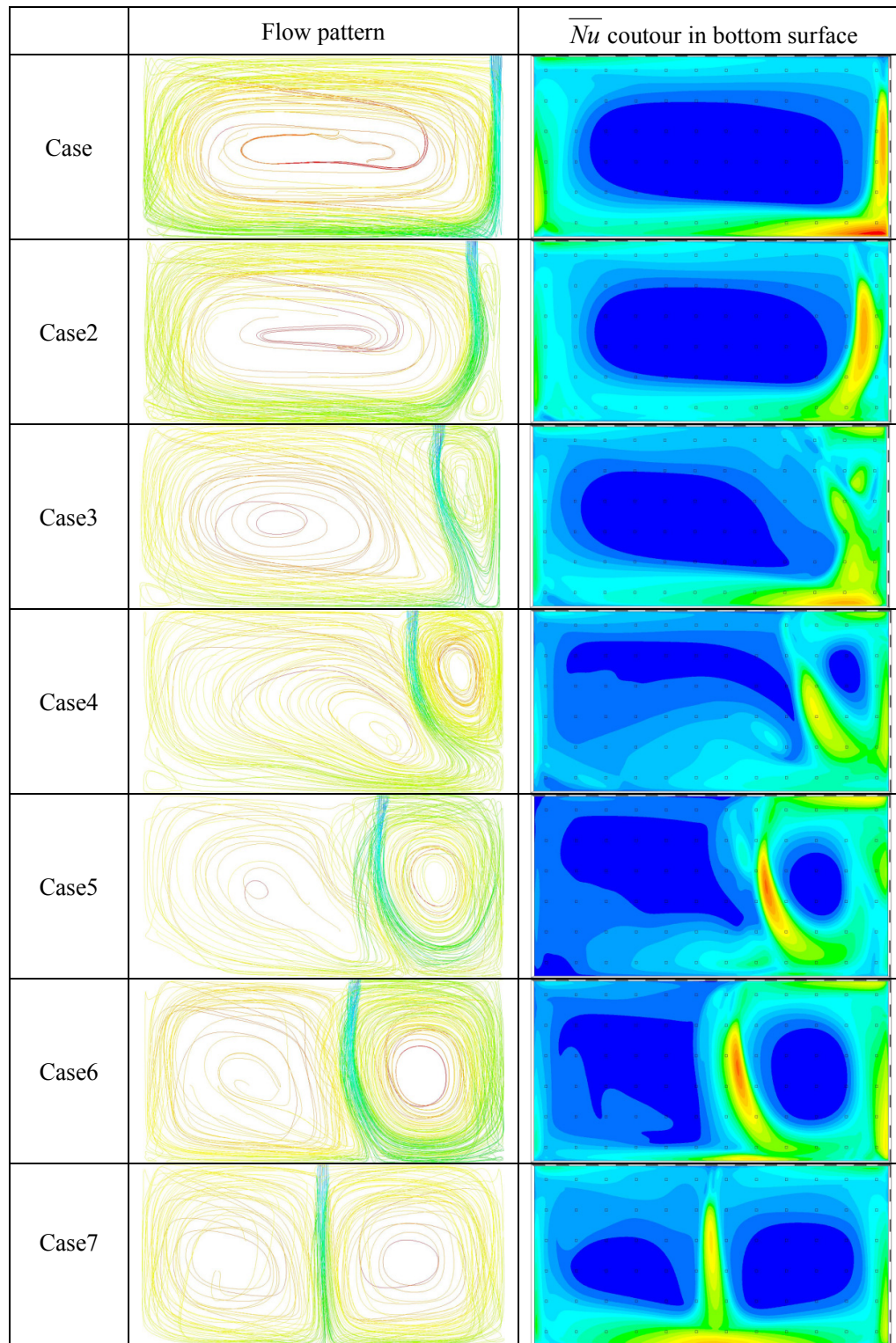


Figure 5.2: The dependence of flow patterns and \overline{Nu} contours on inlet position

The difference between maximum and minimum diffuser temperatures dT at different inlet positions is shown in Figure 5.3 along with the standard deviation of the temperature variance STD. As the inlet position changes, the STD and dT change, but they are not found to be linearly related. Two interesting cases are recognized. For case 4 the dT and STD decreases considerably to reach the minimum values; also for case 7 the dT and STD becomes the second lowest values as shown Figure 5.3.

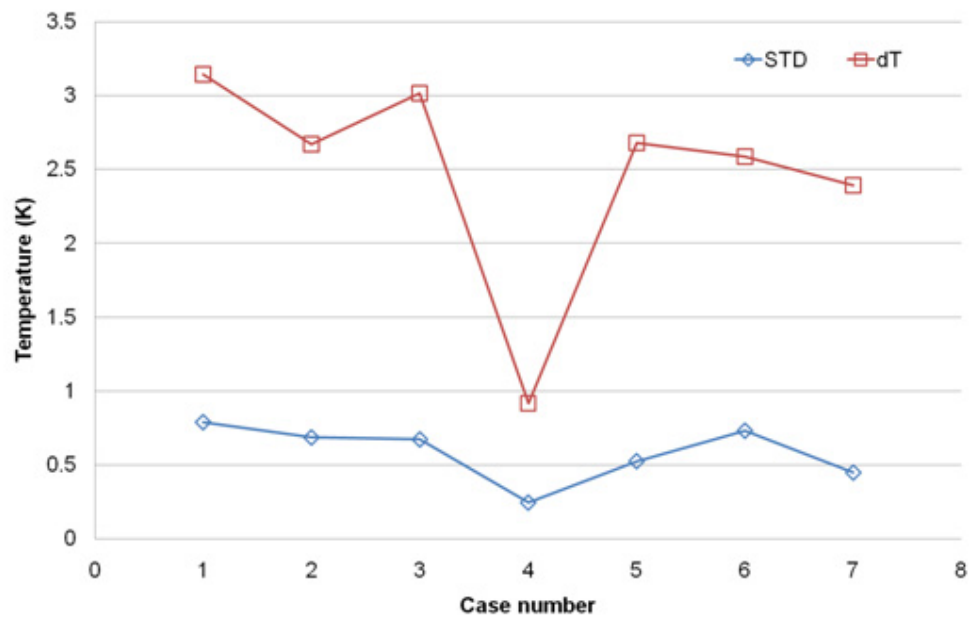


Figure 5.3: The dT and STD of outlet temperatures at each case

The Nusselt numbers for all cases are found to be almost the same as marked as circles in Figure 5.4, and those are compared to previous data.

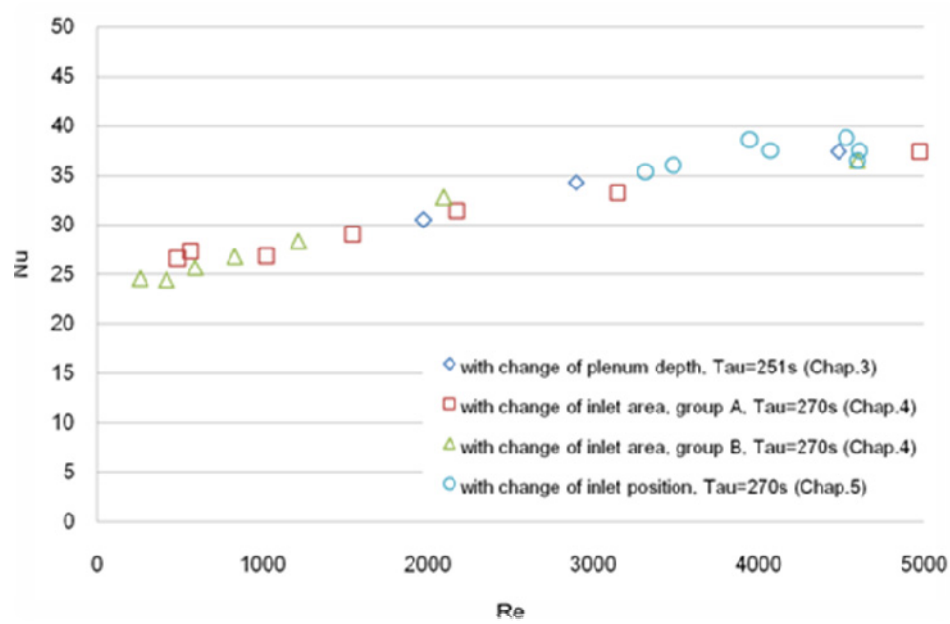


Figure 5.4: The change of \overline{Nu} with \overline{Re} ($\tau = 270s$)

5.2 Summary and discussions

The objective of this chapter is to investigate how the heat transfer and STD of outlet temperatures change with inlet position. With a fixed flow rate only one inlet of $0.01m^2$ is used in each case, and the inlet configuration is described in Figure 4.1. Various flow patterns, which are not intended, are created as shown in Figure 5.2.

When the inlet position is changed, the thermal property of flow are not linearly changed as shown in Figure 5.3. Each particle injected from an inlet is heated with time due to heat conduction started from a slab while the particle moves toward a core with a spiral motion, and the temperature of particle keeps increasing during the travel unless it revisits the mainstream at the end of single circulation. Two cases, case 4 and 7, are found to have lower temperature variations through the diffusers, which is good for the performance of UFAD. Therefore, we tried to

investigate the conditions that make the temperature variation lower in the case 4 and 7.

For the case 4, it is observed that two vortex cores represented by blue circles in Figure 5.5 are located very near to main stream, which enables most of circulating particles to revisit the mainstream. Therefore, the temperature variation of particles becomes the lowest than any other cases.

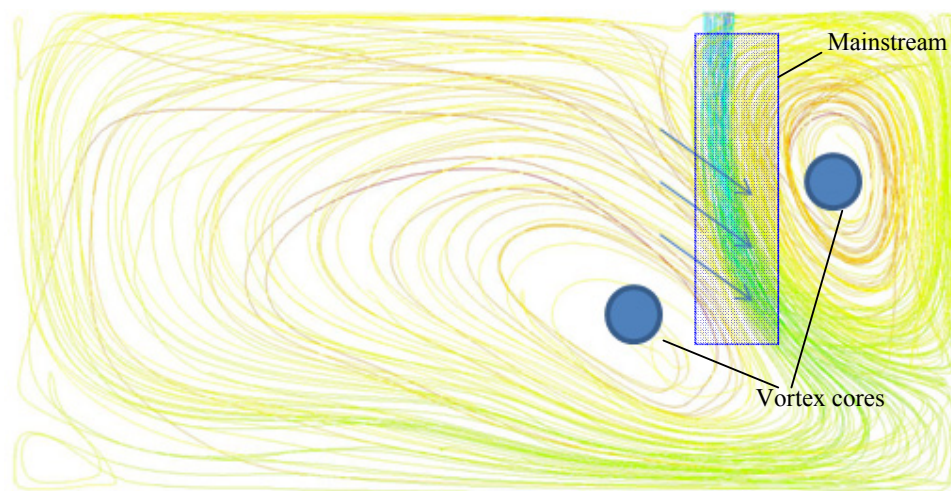


Figure 5.5: Flow pattern created by particle paths for the case 4

For the case 7 it is observed that dT and STD of the outlet temperatures are decreased when a single vortex is separated to two symmetric vortices. In order to confirm the trend we separated a single vortex further to becomes four symmetrical vortices. The inlet configurations are described in Figure 5.5. For the case 3 the inlet is modified to become two angled inlets. The flow patterns and \overline{Nu} contours on the bottom surfaces are drawn in Figure 5.7.



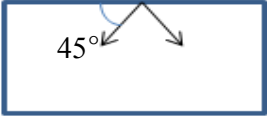
Case number	Open inlet	Inlet configuration
Case 1 $Q=0.02\text{m}^3/\text{s}$	x1	
Case 2 $Q=0.02\text{m}^3/\text{s}$	x7	
Case 3 $Q=0.02\text{m}^3/\text{s}$	x7	

Figure 5.6: Inlet configurations for investigating the effect of number of vortex in a plenum

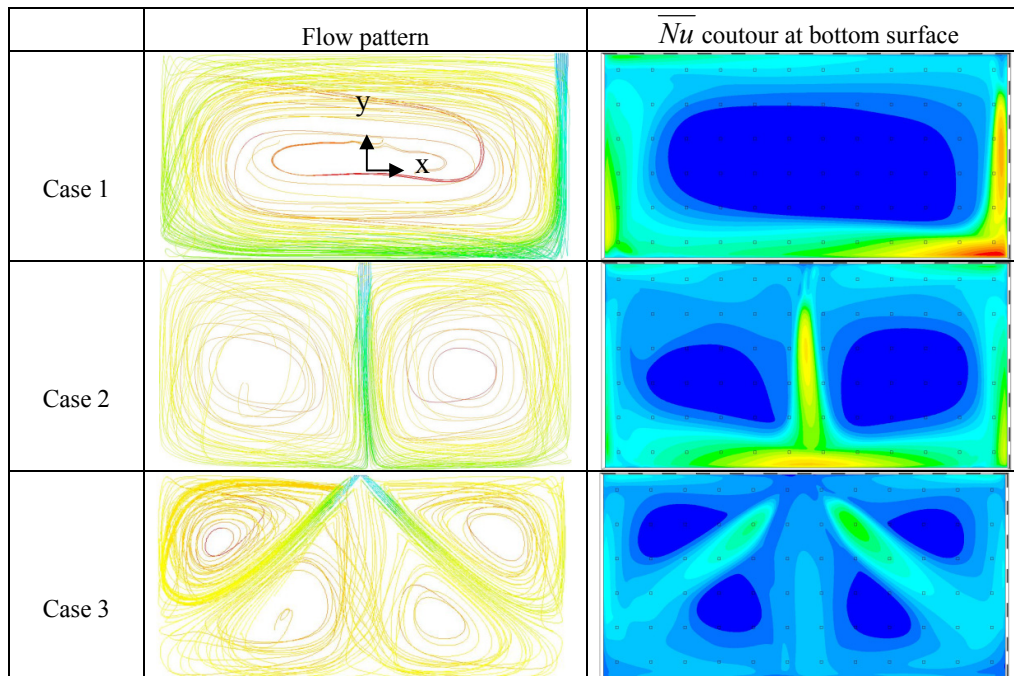


Figure 5.7: The flow patterns and \overline{Nu} contours corresponding to the number of vortices

We define the perimeter as a path that surrounds a unit vortex in each case as indicated in Figure 5.8. It implies a path length required a particle to complete a full circulation.

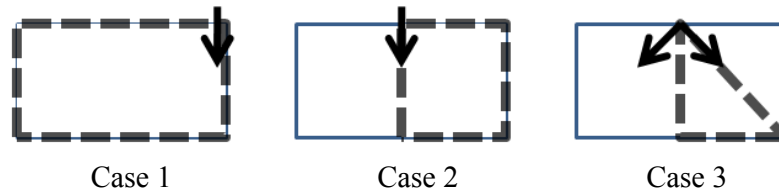


Figure 5.8: A perimeter of unit vortex at each case

We found that the STD and dT are further decreased when the number of vortex is increased to four as shown in Figure 5.9.

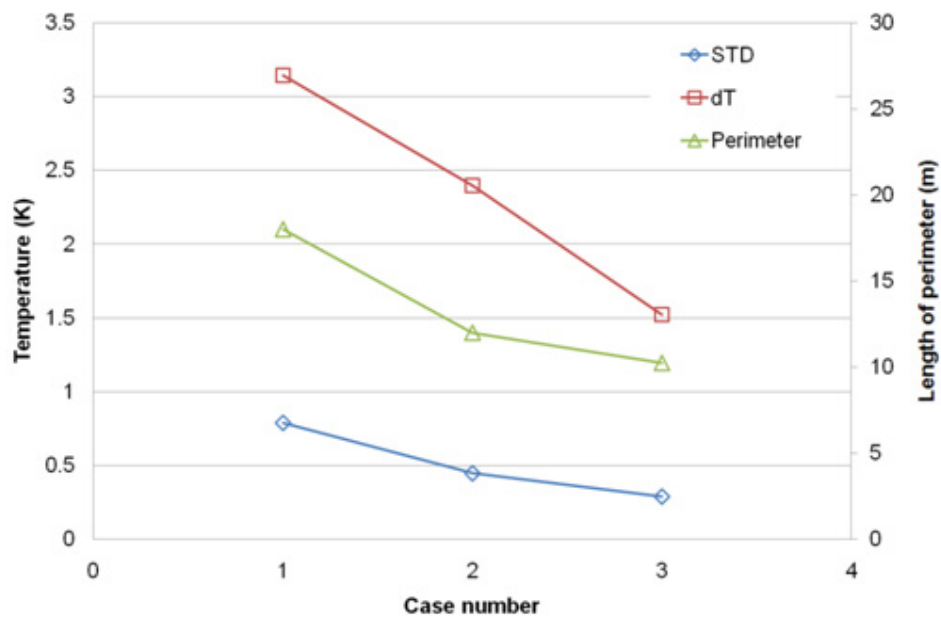


Figure 5.9: The change of dT and STD of outlet temperatures with the number of symmetrical vortices

If the length of perimeter becomes shorter, the time period for a particle to make a full circulation around a unit vortex becomes shorter, which means the

particle may reach a cooling source such as a mainstream more quickly before its temperature gain increases the STD of outlet temperatures. Therefore, the STD of outlet temperatures are decreased when the number of vortices is increased or when the vortex size is decreased.

From the next figures we may confirm that the residence time during a single circulation decreases as the number of vortices increases, and they show the distance of an arbitrary air particle from a y-axis with time, and the periodical motions are detected due to the vortex motions shown in Figure 5.7. For case 1 the arbitrary air particle circulates along its perimeter with a period of 45s. After 250s the particle moves a little toward a core, and the period of circulation is increased.

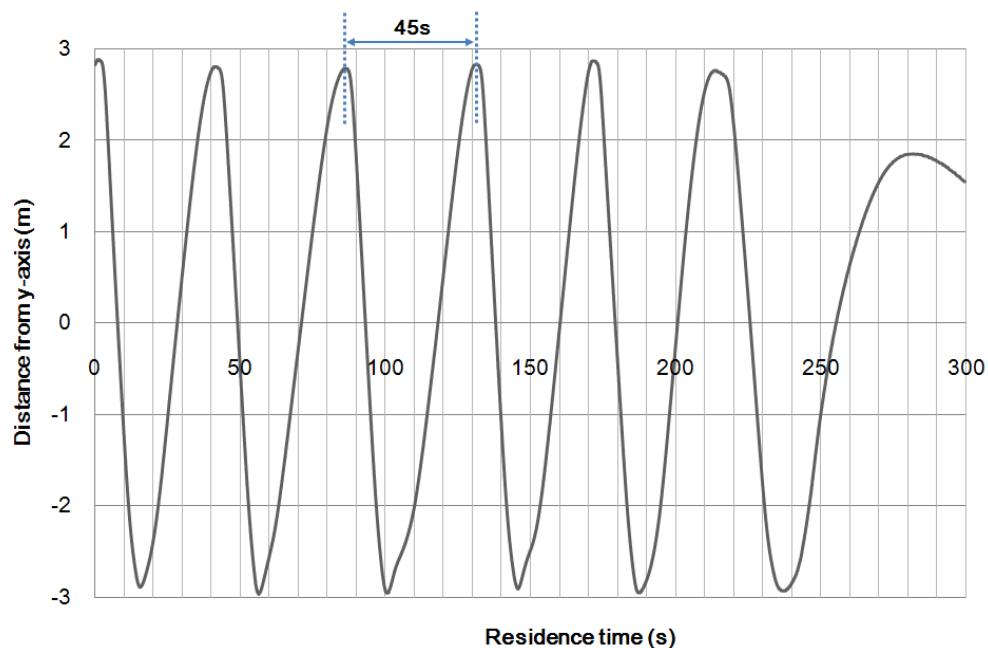


Figure 5.10: The change of distance from y-axis with residence time (Case 1)

For case 2 where a vortex is separated to two symmetrical vortices the time period while a particle travels along its perimeter is decreased to 33 s as shown in Figure

5.11. When the particle circulates near to a vortex core after 200 s the period becomes longer.

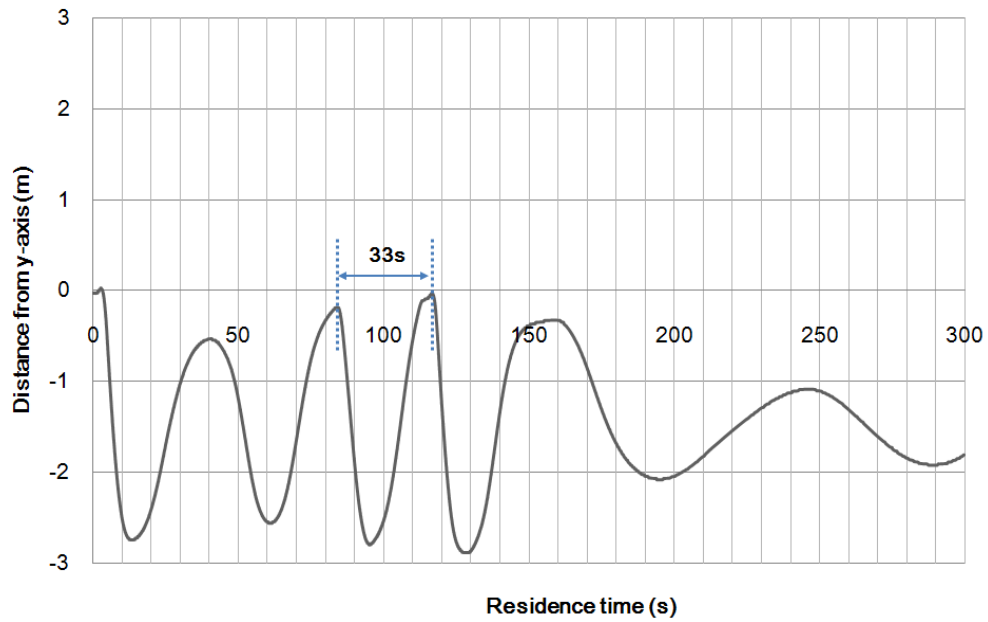


Figure 5.11: The change of distance from y-axis with residence time (Case 2)

For the case 3 the residence time for a particle to circulate along a perimeter is decreased to 26 second when a vortex is separated to four symmetrical vortices as shown in Fig.5.12. The particle is entrained to another vortex at 170 second.

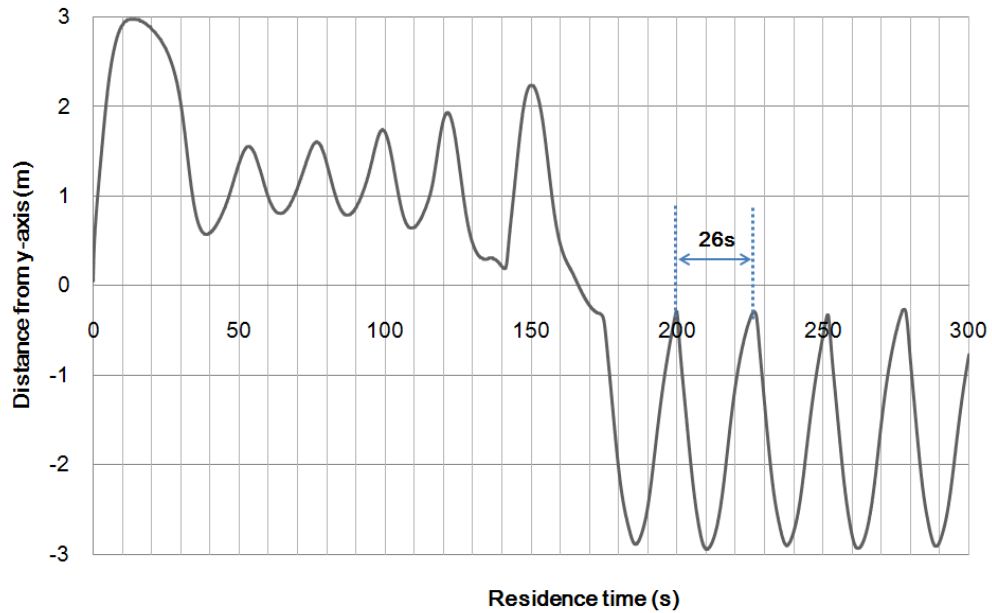


Figure 5.12: The change of distance from y-axis with residence time (Case 3)

We observed that the circulation time decreases as the number of vortices increases, which may account for the fact that the STD of outlet temperatures are decreased when the number of vortices is increased. Another approach to understand the lower STD may be inspired by residence time. In Figure 5.9, Case 1 indicates the highest STD of outlet temperatures, and which may be explained by the spatial temperature difference between inner vortex and perimeter regions (Figure 5.13). As we observed in Figure 3.5 in Chapter 3, the residence time increases as the flow becomes slower. Because the speed of inner vortex region is very slow as shown by velocity profiles in Figure 5.13, the air particle in that region experiences higher residence time as shown in Figure 5.14. Due to heat transfer from a slab, the temperature of the air increases with time, and the higher residence time means the particles is exposed to heat from the lower boundary for longer time. Therefore, the temperature gain of flow in inner vortex region where the particles have more residence time than those in perimeter may become critical.

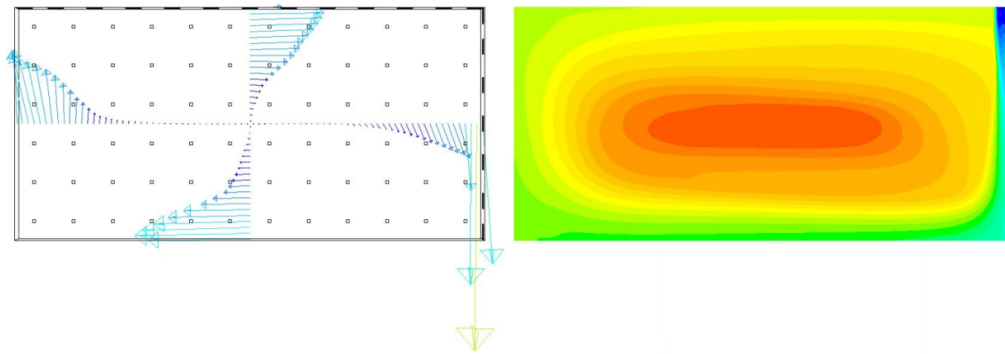


Figure 5.13: The horizontal velocity profile and temperature distribution of flow at mid depth in Case 1 in Figure 5.7

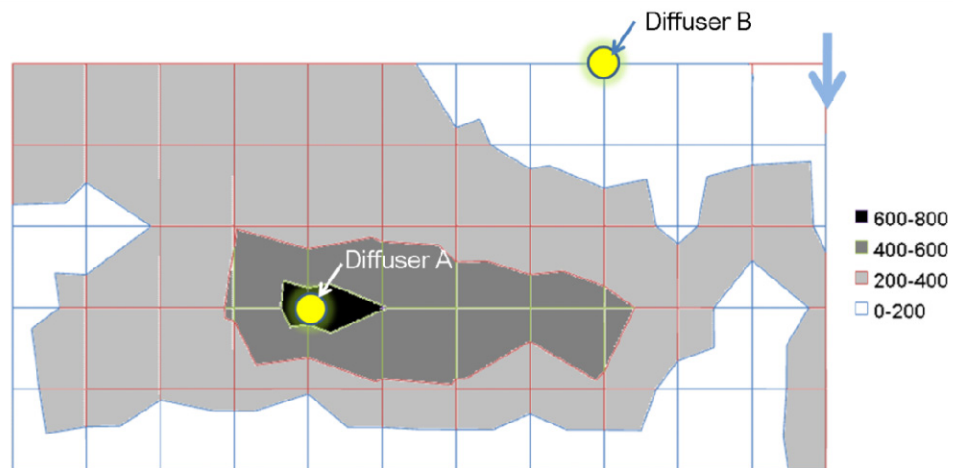


Figure 5.14: The contour of average residence time through diffusers for Case 1 ($\tau = 270$ s) in Figure 5.7. The diffusers are indicated by the spots at which lines are crossed. The range of average residence time is indicated in the legend.

In order to observe the temperature increase of the flow with time corresponding to the position of the outlet, we provide Figure 5.15 in which the temperature change of 70 air particles injected from an inlet and escaped through diffuser A and B are presented. The local average residence times for the particles

which escaped through diffuser A and B were 702 and 102 s, respectively. The behaviors of average temperatures of the particles were shown until the residence times reach to average residence times. The temperature difference between two groups of particles when they escape through diffusers is about 1.5K.

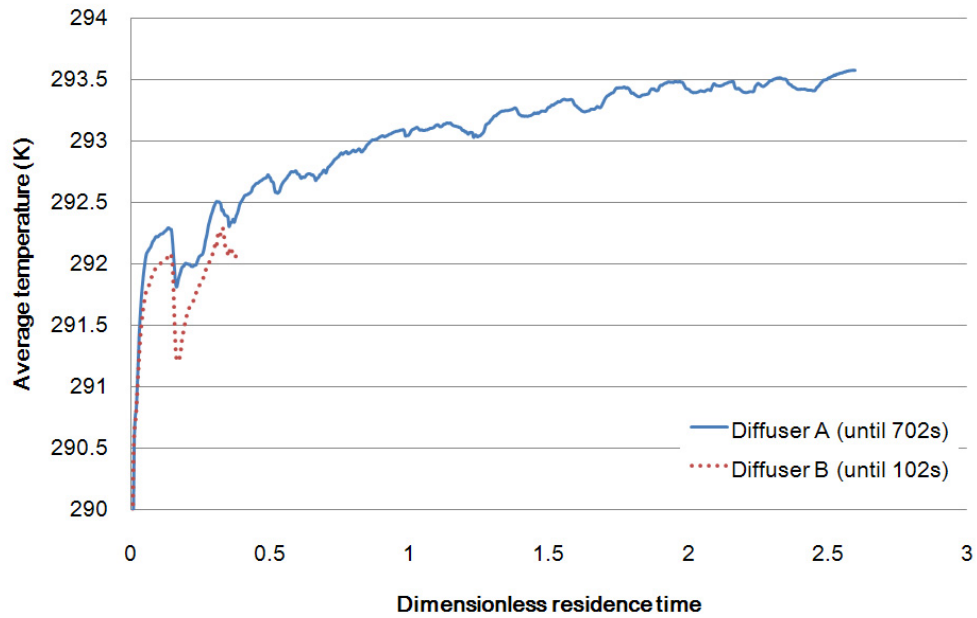


Figure 5.15: The change of temperature of particles with time which escapes through diffuser A and B ($\tau = 270s$)

6 THE EFFECT OF BUOYANCY

6.1 Observations

In the preceding chapters we excluded the vertical motions induced by buoyancy, and we assumed only forced convection is involved in the flow. Now we consider situations for which natural convection effects are added. The buoyancy force is induced by the density gradient due to temperature gradient in the vertical momentum equation, assuming the Boussinesq approximation for density. The objective of this chapter is to obtain an appreciation for the conditions at which a natural convection becomes important, and to examine the flow patterns caused by buoyancy effects. Two sets of simulations were performed. For the first set of simulations we used the one quarter plenum $2.89 \times 2.89 \times H$ m to investigate the effect of buoyancy on heat transfer corresponding to the change of flow rate. For the second set of simulations we fixed the flow rate, but the inlet area is changed as in Chapter 4. The plenum of $3 \times 6 \times 0.3$ m is used to study the effect of buoyancy on the STD of outlet temperatures and heat transfer corresponding to the change of inlet area.

For the first set of simulation where the plenum $2.89 \times 2.89 \times H$ m is used the behavior of average Nusselt number \overline{Nu} with \overline{Re} is represented in Figure 6.1. The cases with buoyancy effects are drawn by solid lines, and the cases with no buoyancy effects are drawn with dashed lines. The average Nusselt number \overline{Nu} increases with \overline{Re} for both the buoyant and non-buoyant cases, but the difference between the two cases is observed to decrease with \overline{Re} . This is because the effects of buoyancy are relatively smaller for larger flow rates and the fraction of the heat

transfer due to natural convection is reduced with \overline{Re} . We observed the average Nusselt number for mixed convection \overline{Nu}_{mixed} becomes almost the same as average Nusselt number for forced convection \overline{Nu}_{forced} when the flow rate reaches $0.015\text{m}^3/\text{s}$ (10ACH in a plenum), therefore the effect of natural convection in the plenum may not important above the flow rate.

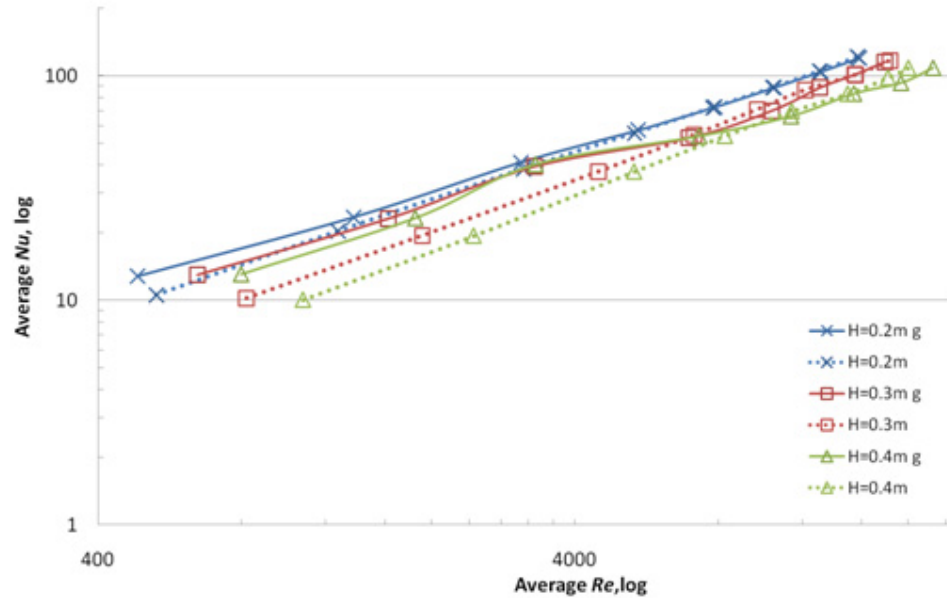


Figure 6.1: The effect of gravity g on \overline{Nu} corresponding to plenum depths

For the second set of simulation where the flow rate was fixed we varied the inlet area to control \overline{Re} . In the previous chapters where only forced convection was considered, it was found that the heat transfer through a slab can be reduced by enlarging inlet area because it decreases \overline{Re} as shown in Figure 4.14. However, when buoyancy is included, the enlargement of inlet area does not guarantee a reduction in the heat transfer because low \overline{Re} triggers additional heat transfer by a natural convection. The ratio $\overline{Gr}/\overline{Re}^2$ gives a qualitative indication of the influence of buoyancy effects on forced convection. $\overline{Gr}/\overline{Re}^2$ is defined by Equation 6.1. Generally, natural convection is negligible when \overline{Gr} is smaller than

\overline{Re}^2 , and forced convection is negligible if \overline{Gr} is bigger than \overline{Re}^2 . Hence the mixed convection occurs usually when $\overline{Gr} / \overline{Re}^2$ is around one (Incropera 2000).

$$\frac{\overline{Gr}}{\overline{Re}^2} = \frac{[g\beta L^3 (T_{top} - T_{bottom})] / \nu^2}{(uH / \nu)^2} \quad (\text{Equation 6.1})$$

This criterion is applied to the cases for an underfloor plenum in order to identify the modes of convection corresponding to inlet areas. After we classify the convection modes we will investigate how the convection modes changed by inlet area affects on heat transfer.

Three groups of simulations were performed. Each group had the same flow rate, and the inlet configuration for each case and dimensionless groups corresponding to the configuration are shown in Table 6.1. The geometry of plenum is described in Figure 4.1. With a fixed plenum geometry and flow rate, we decrease \overline{Re} by increasing inlet area from 0.1m^2 to 0.7m^2 with a increment of 0.1 m^2 . The cases at which $\overline{Gr} / \overline{Re}^2$ is larger than 1 are darkened in the table, and these cases are expected to be dominated by natural convection.

Table 6.1: Inlet configurations and dimensionless groups corresponding to cases

Flowrate (m ² /s)	Case number	Open inlets	Inlet area(m ²)	Ra	Gr	Re	Nu	Gr/Re ²
0.02	1	y1	0.01	1.13E+07	1.62E+07	4.77E+03	42.16	0.71
	2	y1,y2	0.02	1.15E+07	1.64E+07	2.92E+03	42.43	1.92
	3	y1~y3	0.03	1.17E+07	1.67E+07	1.73E+03	42.94	5.57
	4	y1~y4	0.04	1.19E+07	1.70E+07	1.32E+03	43.32	9.71
	5	y1~y5	0.05	1.21E+07	1.73E+07	1.07E+03	44.11	15.17
	6	y1~y6	0.06	1.22E+07	1.75E+07	9.00E+02	44.00	21.59
	7	y1~y7	0.07	1.21E+07	1.74E+07	8.41E+02	44.02	24.56
0.04	8	y1	0.01	9.63E+06	1.38E+07	1.22E+04	72.63	0.09
	9	y1,y2	0.02	9.06E+06	1.30E+07	7.40E+03	67.12	0.24
	10	y1~y3	0.03	8.92E+06	1.27E+07	4.97E+03	66.20	0.52
	11	y1~y4	0.04	9.26E+06	1.32E+07	3.07E+03	67.29	1.40
	12	y1~y5	0.05	8.83E+06	1.26E+07	2.37E+03	66.39	2.24
	13	y1~y6	0.06	9.13E+06	1.31E+07	1.48E+03	67.79	6.00
	14	y1~y7	0.07	9.33E+06	1.33E+07	1.21E+03	69.24	9.16
0.06	15	y1	0.01	8.85E+06	1.26E+07	1.93E+04	98.48	0.03
	16	y1,y2	0.02	7.93E+06	1.13E+07	1.26E+04	88.44	0.07
	17	y1~y3	0.03	7.51E+06	1.07E+07	8.57E+03	83.69	0.15
	18	y1~y4	0.04	7.64E+06	1.09E+07	5.52E+03	83.58	0.36
	19	y1~y5	0.05	7.17E+06	1.02E+07	4.10E+03	79.56	0.61
	20	y1~y6	0.06	7.39E+06	1.06E+07	2.79E+03	81.99	1.36
	21	y1~y7	0.07	8.07E+06	1.15E+07	1.66E+03	89.15	4.21

In the following three figures the average Nusselt numbers \overline{Nu} for the cases with gravity in Table 6.1 are compared with the cases without gravity. The points where $\overline{Gr}/\overline{Re}^2$ is equal to one are marked by small glowing circles. In Figure 6.2 the flow rate is fixed to be $0.02\text{m}^3/\text{s}$ which is equivalent to 13ACH in the plenum. The left side of the circle indicates the region where $\overline{Gr}/\overline{Re}^2$ is larger than one, which imply the effect of natural convection may be dominant.

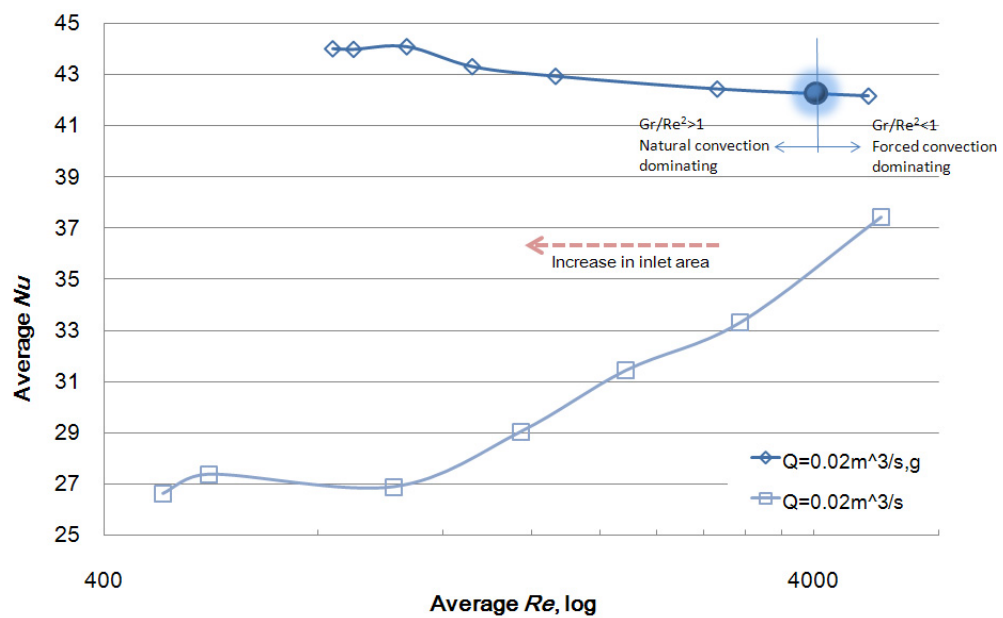


Figure 6.2: \overline{Nu} difference caused by buoyancy effect ($\tau=270\text{s}$ or $Q=0.02\text{m}^3/\text{s}$)

Figure 6.3 represents the case where the flow rate $0.04\text{m}^3/\text{s}$ which is equivalent to 27ACH in the plenum. When a buoyancy force is under consideration, the average Nusselt number \overline{Nu} becomes almost the minimum when $\overline{Gr}/\overline{Re}^2$ becomes one. The right side of a glowing circle represents the forced convection dominant region, therefore \overline{Nu} increases when \overline{Re} increases. The left side of the circle represents the natural convection dominant region, so \overline{Nu} increases as \overline{Re}

decreases because the effect of natural convection grows when the speed of flow becomes slower.

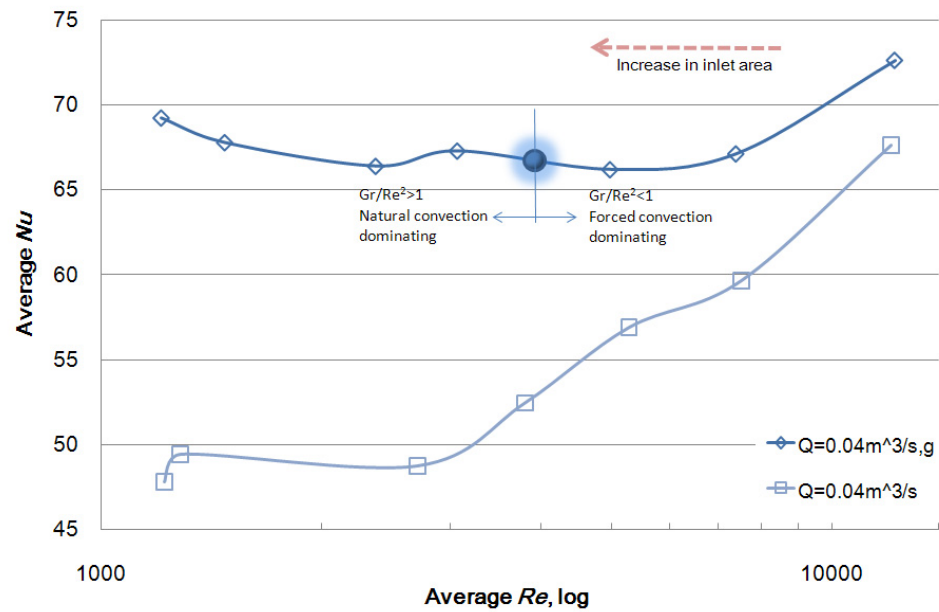


Figure 6.3: \overline{Nu} difference caused by buoyancy effect ($\tau = 135$ s or $Q = 0.04 \text{ m}^3/\text{s}$)

Figure 6.4 shows the case where the flow rate $0.06 \text{ m}^3/\text{s}$ which is equivalent to 40ACH in the plenum. Similarly to previous figures the average Nusselt number \overline{Nu} becomes almost the minimum when $\overline{Gr} / \overline{Re}^2$ reaches to one. The mixed convection region can be identified by the point where $\overline{Gr} / \overline{Re}^2 \approx 1$.

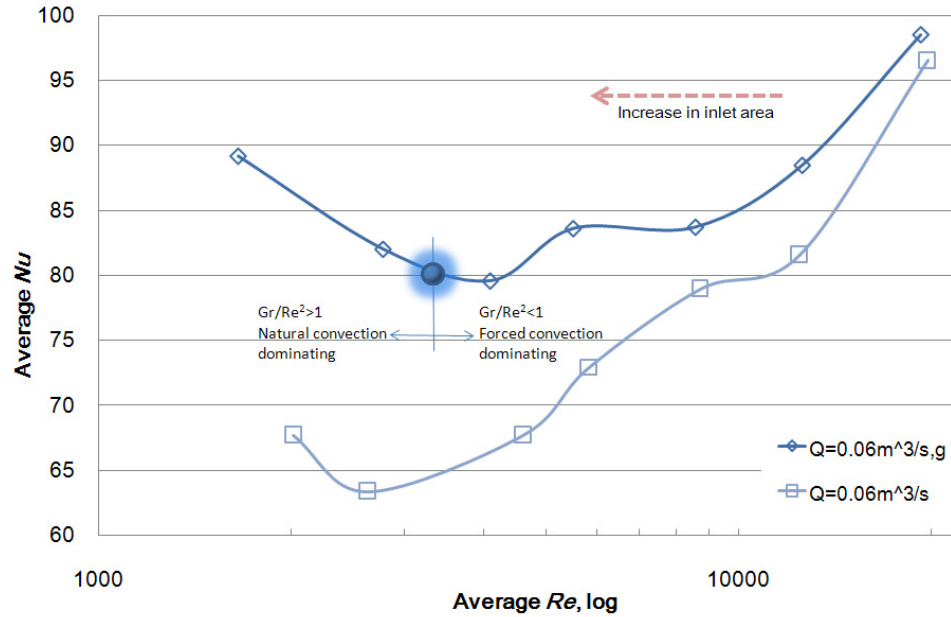


Figure 6.4: \overline{Nu} difference caused by buoyancy effect ($\tau=90s$ or $Q=0.06m^3/s$)

Now we consider the STD of outlet temperatures for the second set of simulations. In Chapters 4 and 5 we have observed that flow patterns are the important factor in controlling the temperature variation of the air leaving through the diffusers. The change of flow pattern by inlet area variation and the effect of buoyancy on flow pattern are shown in Figure 6.5. The left column is the case with no gravity, and the right column is the case with gravity along with Boussinesq approximation for density. The inlet area A is increased from $0.01m^2$ to $0.07m^2$ with a increment of $0.01m^2$.

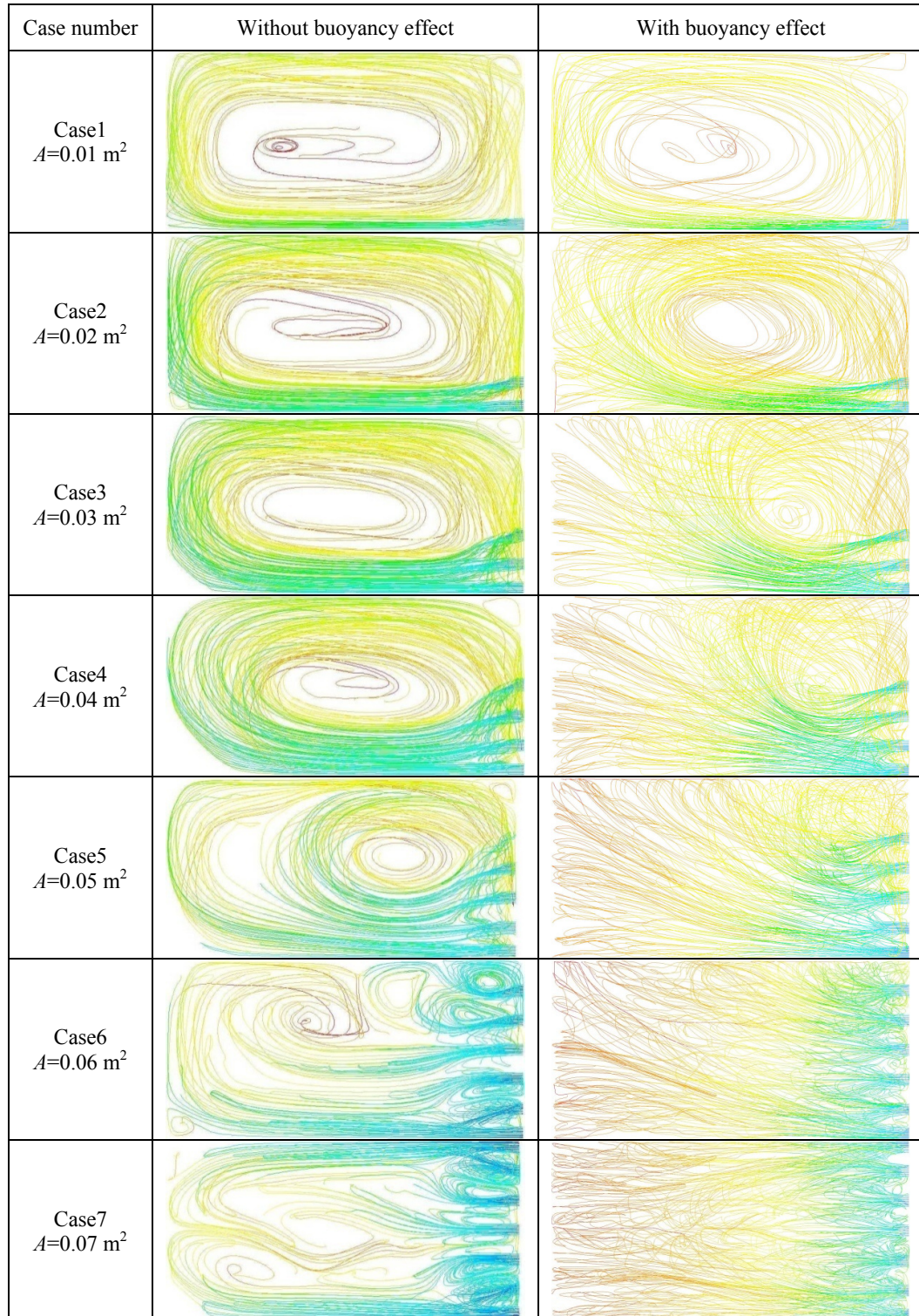


Figure 6.5: The buoyancy effect on the flow patterns ($\tau = 270\text{s}$ or $Q=0.02\text{m}^2$)

The dominant flow for the no-gravity cases was two dimensional motion by forced convection, but the three dimensional vertical motion with a vertical velocity driven by natural convection is detected when buoyancy is added as shown in the right column in Figure 6.5. As the flow speed is decreased by increasing inlet area, it weakens the momentum needed to maintain a vortex pattern. In other words, the buoyancy force helps to lose two dimensional motion so that the vortex pattern is broken more easily compared to no-gravity case, and the change of flow pattern is closely related to the behavior of STD of air temperature at outlets as shown in Figure 6.6. The STD of outlet temperatures is observed to be raised when the vortex pattern is broken.

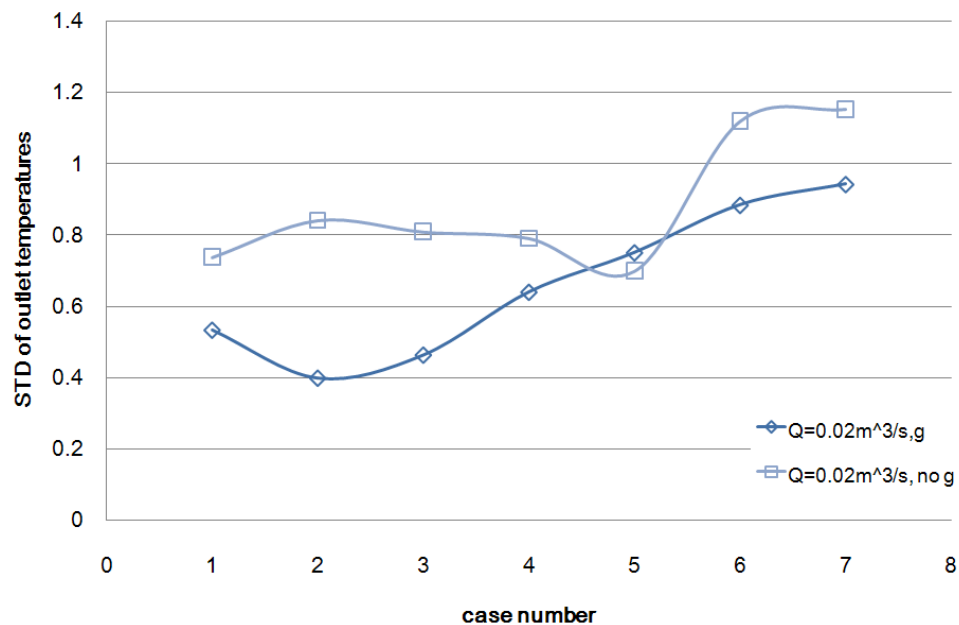


Figure 6.6: STD of outlet temperatures for gravity case and no gravity case

$$(\tau = 270\text{s or } Q = 0.02\text{m}^2)$$

When the flow rate is increased to $0.04\text{m}^3/\text{s}$, the vortex pattern survives further with an increase of inlet area as shown in Figure 6.7. The vortex patterns in both the buoyant and non-buoyant cases are severely disrupted when they reach to case 13.

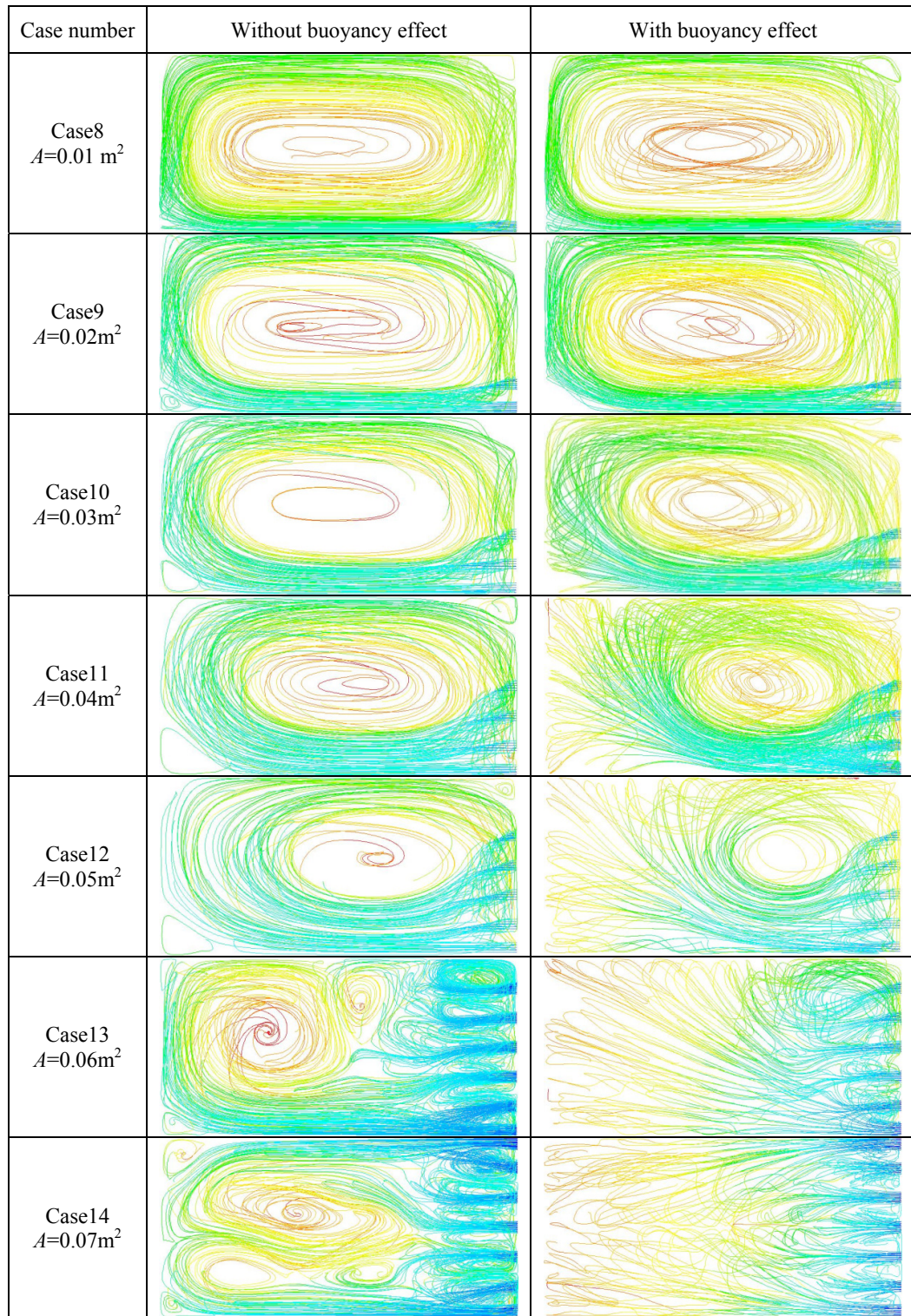


Figure 6.7: The buoyancy effect on the flow patterns ($\tau=135\text{s}$ or $Q=0.04\text{m}^2$)

Figure 6.8 shows that the STDs of outlet temperatures are noticeably increased when the vortex pattern starts to be disrupted by the appearance of vertical motions.

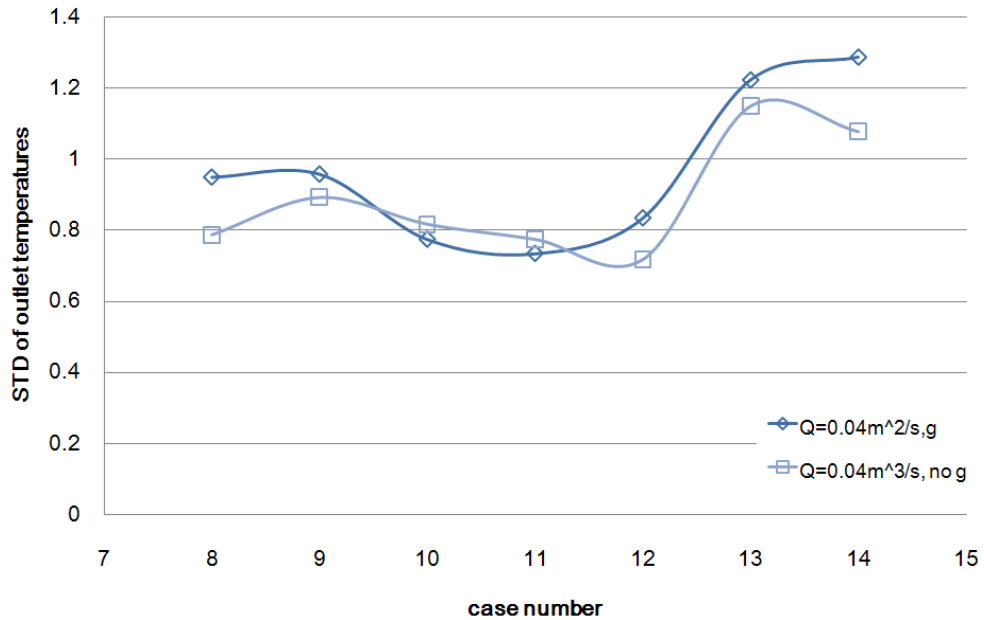


Figure 6.8: STD of outlet temperatures for gravity case and no gravity case ($\tau = 135\text{s}$ or $Q=0.04\text{m}^2$)

When the flow rate is increased to $0.06\text{m}^3/\text{s}$, both cases with and without buoyancy show similar flow patterns as shown in Figure 6.9. In both cases the vortices experience severe distortions when they reaches to case 21.

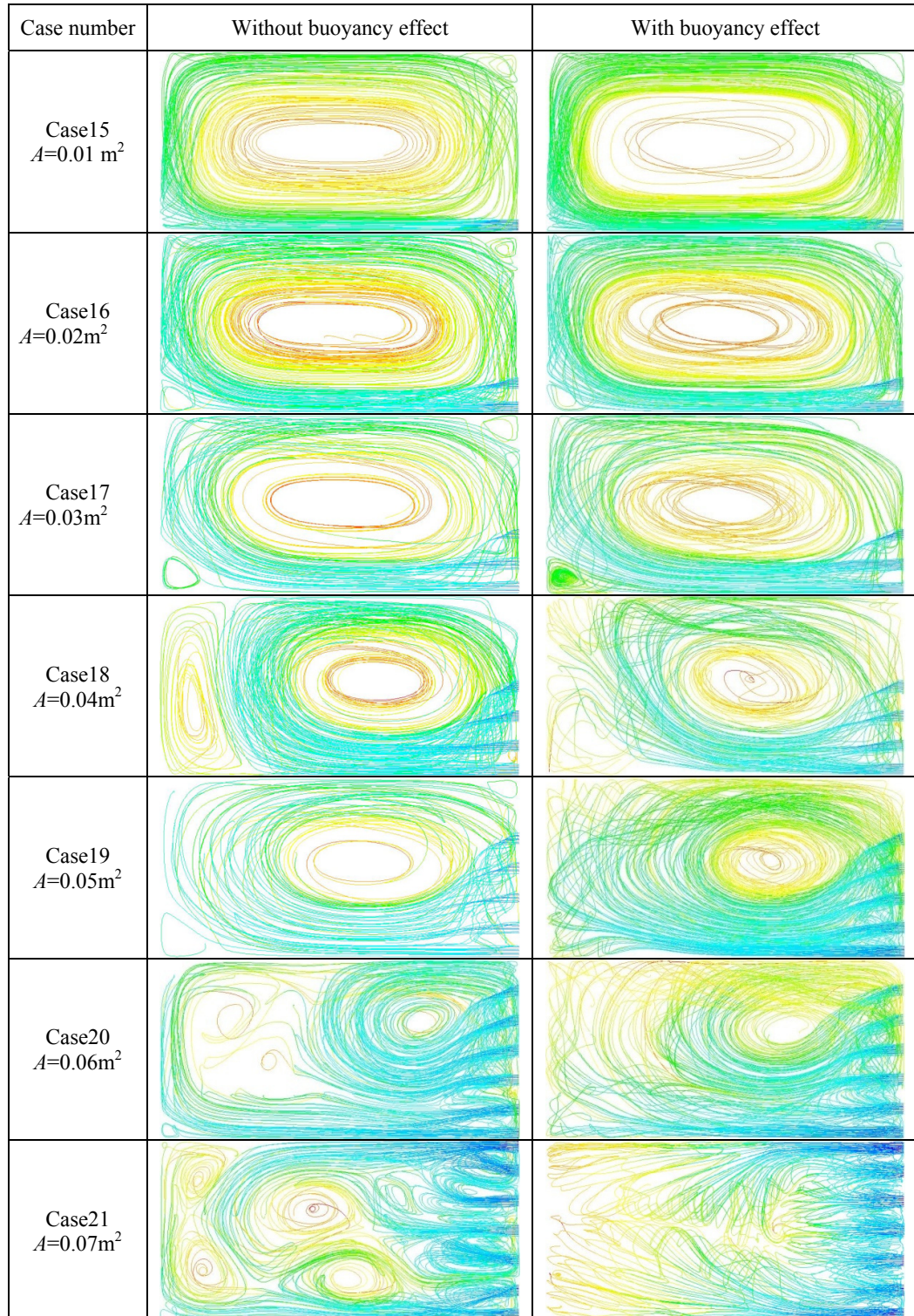


Figure 6.9: The buoyancy effect on the flow patterns ($\tau = 90\text{s}$ or $Q = 0.06\text{ m}^2$)

The STD of outlet temperatures for both cases behaves similarly, but for the case with gravity the fluctuation is steeper than the case without gravity.

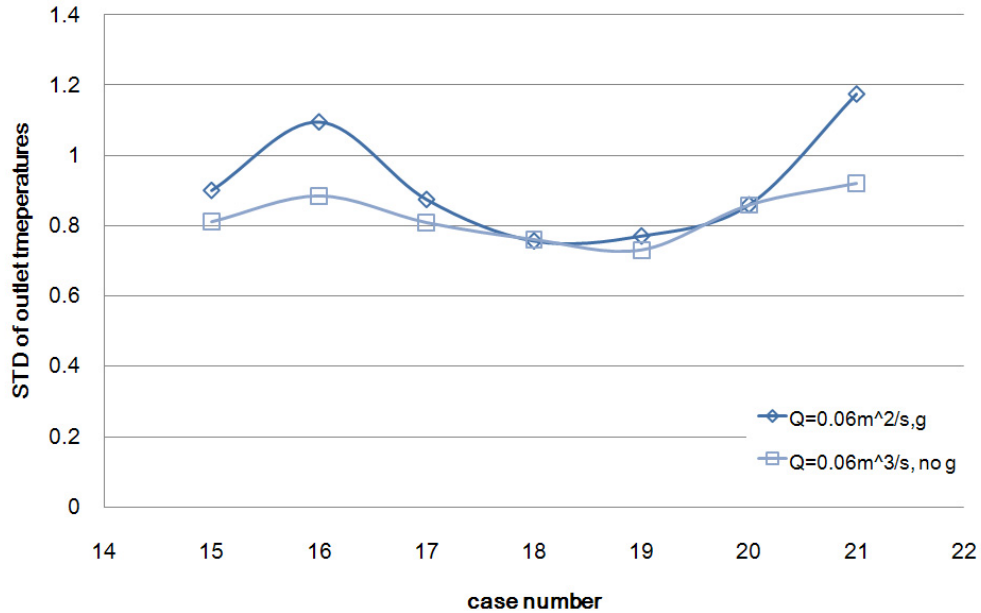


Figure 6.10: STD of outlet temperatures for gravity case and no gravity case

($\tau=90\text{s}$ or $Q=0.06\text{m}^2$)

6.2 Summary and discussions

In this Chapter we have observed the effect of buoyancy on heat transfer and STD of outlet temperatures. From the first set of simulations we increased the average Reynolds number \overline{Re} by increasing flow rate, and we have observed that the fraction of natural convection decreases with flow rate as indicated in Figure 6.1. In the second set of simulations with a constant flow rate we decreased the average Reynolds number \overline{Re} by increasing inlet area. We observed the average Nusselt number \overline{Nu} becomes the minimum when $\overline{Gr} / \overline{Re}^2$ becomes around one, which implies that the heat transfer across a slab caused by mixed convection may be lower than that caused by either natural or forced convection flow. The buoyancy effects

on flow patterns as shown Figure 6.5, 6.7, and 6.9, and we observed the vortex pattern is more easily broken when the buoyancy is considered. When the vortex pattern is broken, the STD of outlet temperatures is observed to decrease.

In order to investigate how the vortex pattern is related to the STD of outlet temperatures we select two critical examples: Case 1 and Case 7 in Figure 6.5. The flow for Case 1 has a circulation pattern, while the flow for Case 7 does not have the pattern, but the entire flow moves to the left from the wall.



Figure 6.11: The flow patterns for Case 1 and 7 ($Q=0.02\text{m}^3/\text{s}$, buoyancy included)

We injected around 70 air particles from an inlet, and observed the change of average temperature of 70 air particles with dimensionless residence time. In Figure 6.12, the average temperature of the particles with vortex pattern (Case 1) fluctuates, and the temperature difference between the flows in low and high residence time regions is small. For the Case 7 the average temperature of the flow without vortex pattern (Case 7) continuously increases with time, and the temperature difference between the flows in low and high residence time regions is significant, which implies the range of temperature in the flow is big. Therefore, we may consider that the STD of outlet temperatures for the flow with circulation is

lower than that for the flow without circulation because the circulation prevents to have critical temperature gain.

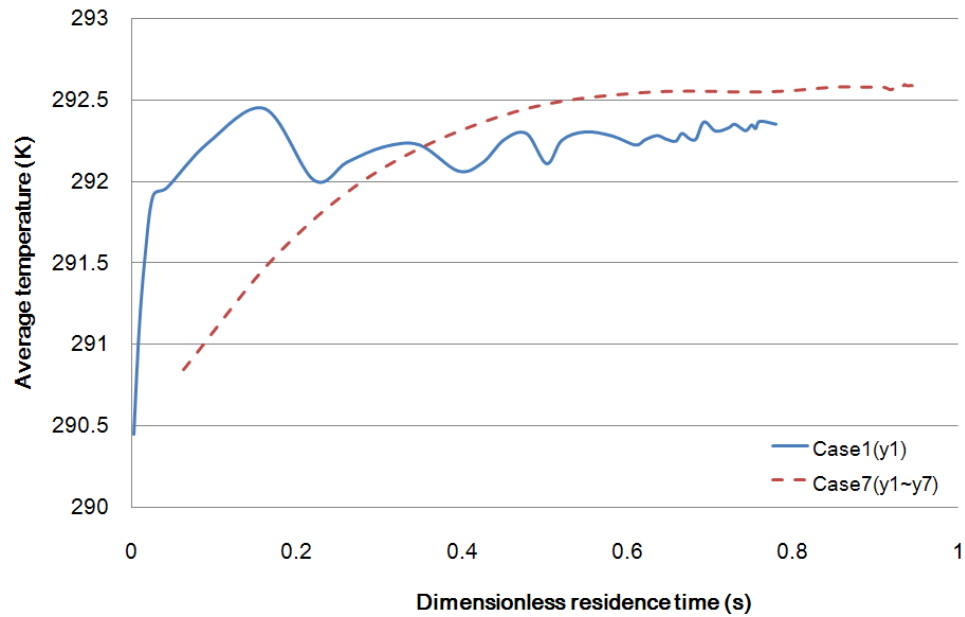


Figure 6.12: The change of average temperature of 70 air particles with dimensionless residence time for case 1 and 7. The open inlet IDs are indicated in parenthesis.

7 CONCLUSIONS

We have observed the flow in a plenum monitoring the behaviors of dependent parameters such as the residence time, path length, average Nusselt number \overline{Nu} , and the STD of temperatures of air particles leaving the plenum through diffusers. The behaviors of the dependent parameters were investigated by CFD calculations of case studies for different values of the independent parameters of plenum depth, flow rate, inlet position, inlet area, and buoyancy effects. The objectives of this thesis are to investigate the properties of flow in a plenum, and provide ideas to reduce the temperature variation of air leaving through diffusers and heat transfer across a slab.

The standard deviation (STD) of outlet temperatures was used to quantify the temperature variation of air in a plenum. We observed the STD of outlet temperatures decreases when the number of vortices increases, or the size of the vortex structure decreases (Figure 5.9). The circulation time, which is defined as the period required a particle to complete a full circulation along a perimeter of vortex, and local residence time, which is defined as time duration for the particles to reside before escaping through local diffuser, were used to account for the observations. As the size of vortex decreases, the circulation time decreases along with a decrease in STD of outlet temperatures (Figure 5.9). The shorter circulation time implies that a particle has more possibility to reach the main stream in a given amount of time. Therefore, a shorter circulation time may help to achieve lower STD of outlet temperatures. The local temperature gain becomes the highest where the local average residence time becomes the highest (Figure 5.14). We found the overall average residence time through all diffusers is almost equal to the replenishment time (Figure 3.7), but the local average residence time of air particles might be

different from the replenishment time because the local residence time depends on local flow speed (Figure 3.5). In addition, the flow speed is mainly determined by flow patterns (Figure 7.1). Therefore, the flow pattern may be a key factor to change the local average residence time. The velocity profiles depending on the number of vortices are shown in Figure 7.1. We observed the flow at the inner vortex region in Case 1 is very slow due to viscous effects on the walls. Therefore, the local average residence time of particles that circulates around the inner vortex region may be longer than that of particles moving around the perimeter of the vortex (Figure 5.14), so the particles near to a vortex core are exposed to heat from the lower boundary for longer time. This may account for temperature gain at inner vortex region and the behavior of STD in Figure 5.9.

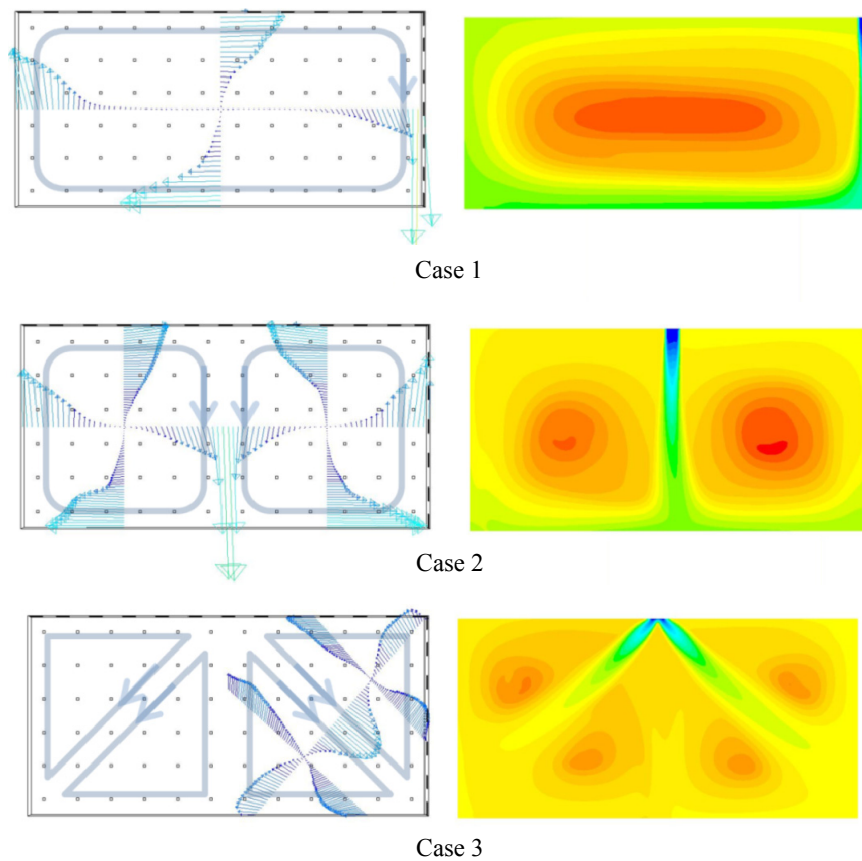


Figure 7.1: The vertical velocity profiles and temperature distribution of flow at mid depth corresponding to the number of vortex or the size of vortex

We have considered the possible conditions for lower STD of outlet temperature by assuming that the flow contains a vortex pattern. When the flow does not have a vortex structure, the flow is continuously moving away from an inlet, and the temperature of flow increases continuously with time without temperature fluctuations (Figure 6.12). Therefore, the temperature difference between the regions near to and away from the inlet becomes higher than that for the flow with a vortex structure, which makes the STD of outlet temperature to increase.

The other objective of the thesis was to reduce heat transfer from the floor below across the floor slab. We have used the average Nusselt number \overline{Nu} on the bottom surface of a plenum to characterize the amount of heat transfer conveyed from a lower story. Without buoyancy effects, the average Nusselt number \overline{Nu} increases with flow rate because an increase in flow rate increases \overline{Re} (Equation 3.5). Also, \overline{Nu} decreases with an enlargement of inlet area because an enlargement in inlet area decreases \overline{Re} (Figure 4.13). Therefore, when the flow rate is fixed, we may have a deduction in \overline{Nu} by increasing inlet area (Figure 4.14). However, when buoyancy effects are taken into consideration, we may lose this advantage because the heat transfer by natural convection becomes important as the \overline{Re} decreases. The average Nusselt number \overline{Nu} is observed to reach the minimum when $\overline{Gr} / \overline{Re}^2 \approx 1$ (Figure 6.2, 6.3, and 6.4), which implies that the heat transfer across a slab caused by mixed convection may be lower than that caused by either natural or forced convection dominant flow.

REFERENCES

- [1] Bauman F., Hui Jin and Tom Webster (2006) Testing and Modeling of Underfloor Air Supply Plenums, ASHRAE Trans., 112(2)
- [2] Zhang, Z., Zhang, W., Zhai, Z. and Chen, Q. (2007) Evaluation of various turbulence models in predicting airflow and turbulence in enclosed environments by CFD: part-2: comparison with experimental data from literature, HVAC&R Res., 13(6), 871-886
- [3] Choudhury D. (1993) Introduction to the renormalization group method and turbulence modeling. Fluent Inc. Technical Memorandum TM-107
- [4] Frank P. Incropera, David P. DeWitt (2002) Fundamental heat and mass transfer, John Willey press